Journal of Structural Geology 191 (2025) 105330

Contents lists available at ScienceDirect

Journal of Structural Geology

journal homepage: www.elsevier.com/locate/jsg

Strain rates recorded in the perimeter-area relationship of recrystallized quartz aggregates from the Sandhill Corner shear zone, Maine, USA

Erik K. Anderson *, Won Joon Song, Scott E. Johnson, Christopher C. Gerbi

School of Earth and Climate Sciences, University of Maine, Orono, ME, 04469, USA

ARTICLE INFO

Keywords:
Quartz
Perimeter-area fractal dimension
Grain boundary migration
Flow laws
Shear zones
Microstructure

ABSTRACT

Current available methods for determining strain rates during viscous deformation are limited, generally relying on the preservation of appropriate microstructures. A lesser-known method to determine strain rates of monomineralic quartz aggregates relates the perimeter-area fractal dimension (D-value) of grain boundaries to deformation conditions. We explore this method by applying it to the Sandhill Corner shear zone (SCSZ), a seismogenic shear zone exhumed from the base of the frictional-to-viscous transition. Strain-rate patterns from D-values are similar to those from flow laws combined with grain size piezometry and predict comparable magnitudes to rates from flow laws using the theoretical piezometer of Shimizu (2012). We compare quartz D-values with proxies for grain shape and grain boundary roughness and find a clear correlation between D-value and grain size, suggesting it may record flow stress. We interpret the disparity in spatial trends between D-value and recrystallized grain size within the inner shear zone as reflecting the influence of transient deformation events associated with the seismic cycle. While the D-value is commonly referred to as a measure of the degree of serration or roughness of grain boundaries, this study suggests a more complex interrelationship of the D-value, grain size, aspect ratio, and roundness. Future field work and experimental calibrations are encouraged to test our findings and refine strain-rate estimates derived from D-values.

1. Introduction

Determination of strain rates in the rock record is important for understanding a range of geologic processes. For example, the rate of metamorphic reactions may be limited by the rate at which rocks accumulate strain (Baxter and DePaolo, 2004). Additionally, strain rates affect the rheology of rocks undergoing viscous flow, controlling (in part) the location and depth of the frictional-to-viscous transition zone (Rolandone et al., 2004). Strain rates across ancient shear zones are commonly inferred from (1) flow laws combined with grain size piezometery (e.g., Luan and Paterson, 1992; Gleason and Tullis, 1995; Hirth et al., 2001; Rutter and Brodie, 2004; Fukuda and Shimizu, 2017; Lu and Jiang, 2019; Tokle et al., 2019; Lusk et al., 2021): or (2) a combination of strain analyses and geochronology (e.g., Christensen et al., 1989; Müller et al., 2000; Sassier et al., 2009; Lusk and Platt, 2020; Cawood and Platt, 2021). Within quartz-rich rocks, geochronometers are limited, and the application of flow laws requires a combination of microstructural analysis, grain size piezometry, and estimates of deformation temperature extracted from geothermometers, quartz recrystallization mechanisms, and/or quartz c-axis opening angles (e.g., Stipp et al., 2002; Stipp and Tullis, 2003; Kidder et al., 2012; Law, 2014; Faleiros et al., 2016). As quartz is commonly considered to strongly influence the strength of the middle and upper continental crust, having an additional strain-rate meter for quartz-rich rocks would be useful in comparing and validating our current understanding of geologic strain rates.

An alternate method for estimating strain rate in the geologic record from monomineralic quartz aggregates was proposed by Takahashi et al. (1998). By measuring the perimeter-area fractal dimension (D-value) of the shape of dynamically recrystallized quartz grains, Takahashi et al. (1998) used an experimental dataset of seven samples (three from Masuda and Fujimura (1981), and four unpublished samples from the same experiments) to establish a relationship among the D-value, strain rate $\dot{\varepsilon}$ (s^{-1}), and temperature T (K) (Fig. 1a). Similar relationships have been observed in metals undergoing viscous creep (Hornbogen, 1987, 1989). Substantial work has been conducted in the material science and metallurgy literature demonstrating the effects of deformation and annealing on the fractal dimension of grain boundaries (e.g., X. Wang

* Corresponding author.
E-mail addresses: erik.k.anderson@maine.edu (E.K. Anderson), wonjoon.song@maine.edu (W.J. Song), johnsons@maine.edu (S.E. Johnson), christopher.gerbi@maine.edu (C.C. Gerbi).

https://doi.org/10.1016/j.jsg.2024.105330
Received 15 February 2024; Received in revised form 21 November 2024; Accepted 7 December 2024
Available online 9 December 2024

et al., 1990; Streitenberger et al., 1995; Tanaka et al., 1998; Z. Wang et al., 2010; Bigerelle et al., 2012). Z. Wang et al. (2010) showed relationships between the recorded fractal dimension and recrystallized grain size as a function of drawing speed (Fig. 1b) and annealing temperature (Fig. 1c). With increasing drawing speed, D-values increase and recrystallized grain sizes decrease, while D-values decrease and grain sizes increase with increasing annealing temperature. Additionally, correlations between the fractal dimension and material properties such as fracture toughness and creep strength have been noted (e.g., Tanaka and Iizuka, 1991; Watanabe and Tsurekawa, 2004), providing a potential avenue to link bulk material properties to fractal microstructures.

Although several geologic studies have employed the perimeter-area fractal dimension (e.g., Mamtani, 2010; Liang et al., 2015, 2017; Ghosh et al., 2016; Sato et al., 2020; Hu et al., 2021; Kalita et al., 2022), they did not explicitly interrogate the method. Additionally, their strain-rate estimates using the perimeter-area fractal dimension (henceforth referred to as the grain boundary dimension (GBD) method) showed up to seven orders of magnitude faster rates than those calculated from some flow laws combined with grain size piezometery (e.g., Liang et al., 2015, 2017; Hu et al., 2021), but this discrepancy has yet to be explored. In this study, we explore the potential uses and limitations of the GBD method by applying it to the Sandhill Corner shear zone (SCSZ), Maine, USA, a well-studied mid-crustal seismogenic shear zone exhumed from the base of the frictional-to-viscous transition. We compare spatial patterns and magnitudes of strain rates estimated from D-values and recent flow laws combined with grain size piezometery. Additionally, we compare D-values to common measurements of grain shape and grain boundary roughness (e.g., perimeter-area fractal dimension, aspect ratio, circularity, and roundness) and explore relationships between them in our field area to better understand its geometric significance. Finally, we explore the impact of variations in deformation mechanisms on the D-value and recrystallized grain size in our field area.

2. Methods

2.1. Grain shape analysis

There is ambiguity in the literature regarding the physical significance of the D-value as it pertains to the geometric properties of dynamically recrystallized quartz aggregates. The D-value is commonly described as a measure of the degree of serration or "roughness" of grain boundaries (e.g., Hornbogen, 1989; Takahashi et al., 1998; Takahashi and Nagahama, 2001), where aggregates of the same shape (e.g., circles, ellipses, or convex polygons) with different sizes have a D-value of unity, and increasing serration with increasing size causes D-values to increase. However, Takeshita and El-Fakharani (2013, their supplement) compared measurements of D-values with a proxy for grain boundary roughness defined by the average normalized ellipse perimeter ($\overline{P}_{norm}$) and concluded that the D-value is not a reliable indicator of grain boundary roughness. To be thorough with our analysis of D-values, we define the shape properties employed in this study (i.e., aspect ratio, circularity, roundness, and $\overline{P}_{norm}$) and their physical significance in Appendix A and summarize them in Fig. 2. We emphasize here that the GBD method simply relates to the measured perimeter and area of a 2D aggregate and is not necessarily an explicit measure of boundary roughness.

2.1.1. Perimeter-area fractal dimension

The geometry of irregular, non-Euclidean shapes can be well-characterized using fractal analysis. While several methods exist to characterize the dimensionality of these surfaces (e.g., ruler and box methods), we restrict the current study to the perimeter-area method (Mandelbrot, 1977). The perimeter-area fractal dimension is determined by measuring the individual grain perimeters in monomineralic polycrystalline aggregates and the equivalent diameter of circles containing the same area as the measured grains (Fig. 2a–c). The reason why the

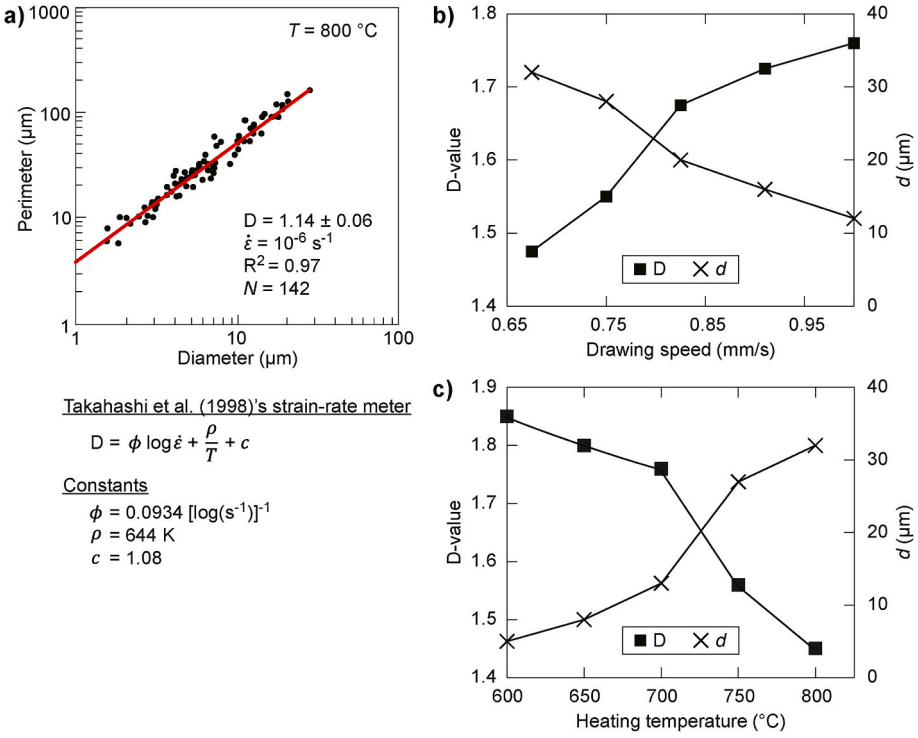

Fig. 1. Previous work on the perimeter-area fractal dimension (D-value). (a) Log-log plot of perimeter versus diameter for recrystallized grains of a sample from the deformation experiments used in Takahashi et al. (1998). The D-value (D) was calibrated to deformation conditions (strain rate $\dot{\varepsilon}$ and temperature T) from seven experimental samples. N is the number of measured grains. (b, c) Correlations between the D-value (D; squares) and recrystallized grain size (d; crosses) in QSi3-1 bronze silicon alloy as a function of drawing speed and heating temperature, respectively. Adapted from Z. Wang et al. (2010). (For interpretation of the references to colour in this figure legend, the reader is referred to the Web version of this article.)

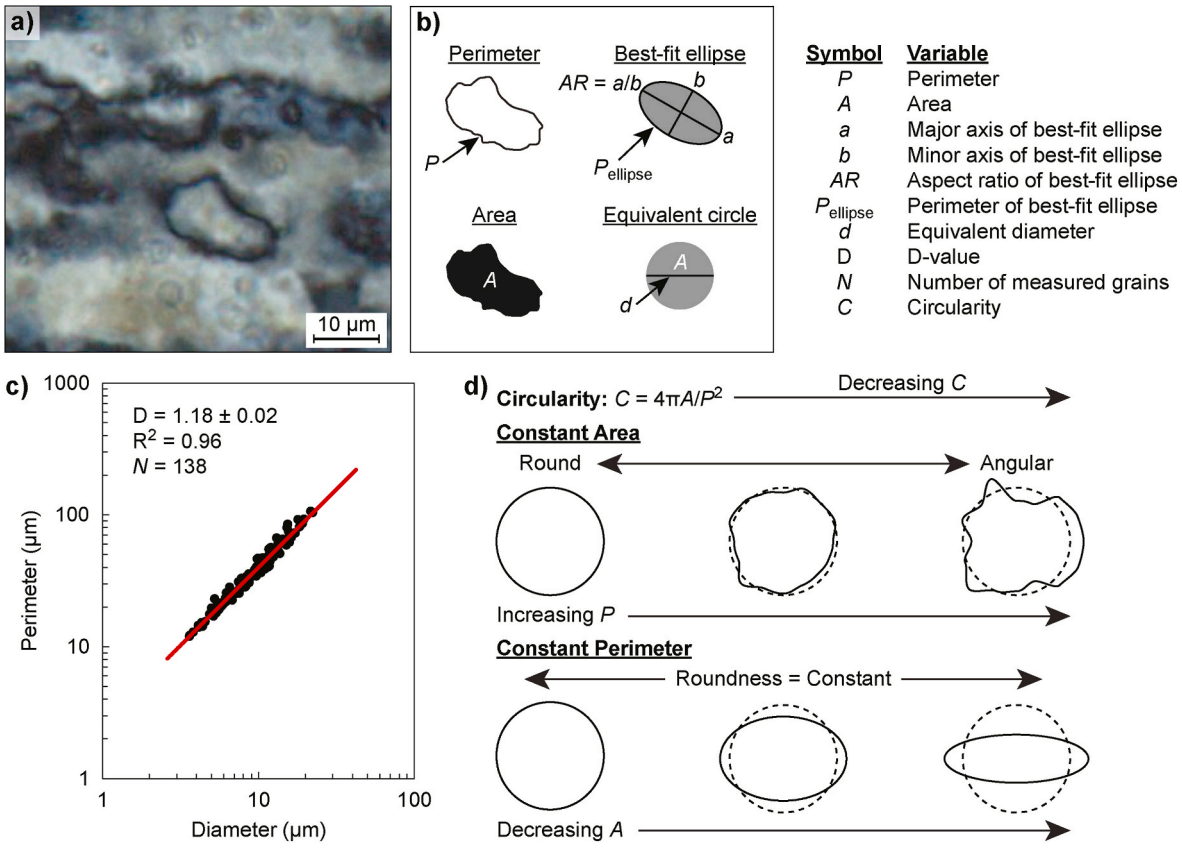

Fig. 2. Definition of D-value and other shape properties. (a) Photomicrograph in cross-polarized light of a recrystallized quartz vein as an example (sample 76). (b) Definition of traced grain and associated variables used in the present study. (c) Log-log plot of perimeter versus diameter for recrystallized quartz grains measured in sample 76 as an example. The power-law relationship is indicated by the best-fit line in log-log space. The D-value corresponds to the slope of the line. (d) Schematic illustration showing the relationship between circularity and roundness. The top panel shows the effect of increasing the perimeter of a circle at constant area. Both circularity and roundness decrease. The lower panel shows the effect of decreasing the area of a circle at constant perimeter, producing a higher aspect ratio. Circularity decreases while roundness is constant. Adapted from Takashimizu and Iiyoshi (2016).

equivalent diameter is plotted despite the use of area in the name of the method stems from the significance of the equivalent diameter of dynamically recrystallized aggregates as a proxy for flow stress through a grain size stress piezometer. The equivalent diameter (d) of each grain is calculated from $d = 2\sqrt{A/\pi}$, where A is the area. The slope of the line in log equivalent diameter (d) versus log perimeter (P) space yields the fractal dimension (e.g., Fig. 2c). Because the range of grain sizes in recrystallized quartz aggregates generally does not span more than ~1 order of magnitude, we refer to the perimeter-area fractal dimension as the "D-value" to avoid the implication of a true fractal relationship that spans several orders of magnitude (Hornbogen, 1989). The D-value of a surface in two dimensions varies between 1 and 2, with values closer to 1 approximating perfect circles and greater values displaying increasing perimeter length for a given area either by an increase in higher frequency boundary roughness or a macroscale shape change such as increased ellipticity (Fig. 2d).

2.2. Strain rate calculation using D-values

Strain-rate estimates derived from D-values were calculated from the empirically derived relationship of Takahashi et al. (1998):

$$D = \phi \log\dot{\varepsilon} + \frac{\rho}{T} + c \tag{1}$$

where $\phi = 0.0934\ [\log(s^{-1})]^{-1}$, $\rho = 644$ K, and $c = 1.08$. In the present study, strain rates calculated from D-values and flow laws combined with grain size piezometers assume a temperature of 400 °C based on estimates from observed quartz microstructures and c-axis opening angles within the shear zone (see Section 3.3 for details) and a confining pressure of 300 MPa based on peak pressure estimates prior to deformation of 300–400 MPa (West et al., 2003).

2.3. Flow stress calculations from grain size piezometry

Differential stress estimates used in strain-rate calculations can be determined using the grain size piezometers of Stipp and Tullis (2003) and Shimizu (2012) listed respectively below:

$$\bar{d} = 3631\sigma^{-1.26} \text{ or } \sigma = 669\bar{d}^{-0.79} \tag{2a}$$

$$\bar{d} = 998\sigma^{-1.25}\exp\left(\frac{12.4\ \text{kJ/mol}}{RT}\right) \text{ or } \sigma = 251\bar{d}^{-0.8}\exp\left(\frac{9.92\ \text{kJ/mol}}{RT}\right) \tag{2b}$$

where $\bar{d}$ is the average recrystallized grain size in μm and σ is the flow stress in MPa. The piezometer of Stipp and Tullis (2003) detects no temperature dependence on the relationship between grain size and flow stress. However, the theoretical piezometer of Shimizu (2012) predicts a weak temperature dependence. We explore the results of using flow stresses from both the piezometers of Stipp and Tullis (2003) and Shimizu (2012) on strain rate estimates (see Section 5.3 for discussion).

2.4. Flow law parameters used for strain-rate calculations

Our understanding of the viscous strength of the continental crust is constrained in part by deformation experiments on quartz aggregates (e.g., Bürgmann and Dresen, 2008). Since the mid-1990s, the empirically derived flow law used to describe the behavior of polycrystalline aggregates undergoing dislocation creep commonly takes the form:

$$\dot{\varepsilon} = A\sigma^n f_{H_2O}^m \exp\left(\frac{-Q}{RT}\right) \quad (3)$$

where $\dot{\varepsilon}$ is strain rate, A is a preexponential factor, σ is the differential stress, n is the stress exponent, f_{H_2O} is the water fugacity, m is the fugacity exponent, Q is the activation energy, R is the universal gas constant, and T is the absolute temperature. We note that while Q is commonly referred to as activation enthalpy in the rock mechanics literature, the thermodynamic definition relates activation energy to the activation enthalpy through:

$$Q = H + pV \quad (4)$$

where H is the activation enthalpy, p is the pressure, and V is the activation volume. The effect of pressure on the activation energy is commonly omitted in the literature due to relatively small values of pV, leading many authors to use activation energy and activation enthalpy interchangeably. In this paper, we maintain the use of Eq. (4), noting that this does not change the results of strain-rate calculations.

Due to the long timescales of rock deformation in nature, laboratory deformation experiments must be performed at elevated temperatures and strain rates to determine flow law parameters on human timescales. However, small adjustments in the experimentally determined flow law parameters can result in large uncertainties when extrapolated to slower geologic conditions. Lusk et al. (2021) used a Markov chain Monte Carlo statistical analysis to determine "naturally constrained" flow law parameters that best fit experimental data on wet quartz aggregates and the deformation conditions in the Whipple mountains core complex of Platt and Behr (2011) and the Scandian shear zone of Lusk and Platt (2020). To eliminate the effect of confining pressure, they separated the compiled data set into low-pressure and high-pressure groups. We choose to include the low-pressure flow law of Lusk et al. (2021) best suited for the conditions of our field area (i.e., that of the middle crust).

Tokle et al. (2019) similarly compiled experimental data from "water-added" deformation experiments on quartz aggregates undergoing dislocation creep and observed two trends with varying stress exponent with "low-stress"/high-temperature data exhibiting $n = 4$ and "high-stress"/low-temperature data exhibiting $n = 2.7$. These trends were correlated with c-axis fabrics indicative of easy slip on prism <a> and basal <a> systems, respectively, with the transition between the two suggested to occur by dislocation-accommodated grain boundary sliding. Using their laboratory fits, they tuned their parameters to match the field-based constraints from the Whipple mountains metamorphic core complex and the Ruby Gap duplex. In the SCSZ, the pervasiveness of fluids within quartz veins and the observation of c-axis fabrics indicative of prism <a>/rhomb <a> slip within quartz aggregates support our use of their $n = 4$ experimental flow law fit extrapolated to geologic conditions (Price et al., 2016; W.J. Song et al., 2020b; see Section 3 for description of quartz microstructures).

Lu and Jiang (2019) pointed out that while the incorporation of water fugacity into flow laws in the mid-1990s helped rectify discrepancies between the strength of some experimental data at high temperatures, these discrepancies reemerged when extrapolated to lower temperature conditions found in the middle crust. They hypothesized that pressure not only affects the viscous strength of quartz aggregates through the fugacity term, but that it becomes important through the pV term in Eq. (4) at lower temperatures. By considering only high-resolution steady-state deformation experiments on quartz aggregates exhibiting regime 2/3 microstructures (i.e., deforming by subgrain rotation recrystallization), they determined a set of flow law parameters, including the activation volume, best constrained by three experimental studies. Lusk et al. (2021) additionally considered activation volume in their flow law. Because quartz microstructures in our field area exhibit dominant recrystallization by subgrain rotation recrystallization (see Section 3 for quartz microstructures), we include the experimental flow law of Lu and Jiang (2019) in the discussion. We note here that while other treatments and corrections of flow laws that consider additional factors such as the stress corrections proposed by Holyoke and Kronenberg (2010) exist (e.g., Fukuda and Shimizu, 2017), the proposed correction is a source of ongoing debate and has not been used in recent studies (see Tokle et al., 2019; Lusk et al., 2021 for discussion). In this study, we tentatively test the flow laws determined by Lusk et al. (2021), Tokle et al. (2019), and Lu and Jiang (2019), and provide their forms and parameters in Table 1.

The water fugacity in this study was estimated from the empirical fit of a thermodynamic database (Pitzer and Sterner, 1994) that provides a good fit of fugacity across a range of crustal geotherms, taking the form:

$$f_{H_2O} = a_{H_2O} A_1 \exp\left(\frac{-(A_2 + pA_3)}{RT}\right) \quad (5)$$

where a_{H_2O} is the activity of water (here taken to be unity assuming that our samples are water saturated, which may be validated by the pervasiveness of fluid inclusions within quartz veins across the SCSZ as shown in W.J. Song et al., 2020b), $A_1 = 5521$ MPa, $A_2 = 31.28$ kJ/mol, and $A_3 = -2.009 \times 10^{-5}$ m^3/mol (Shinevar et al., 2015). By assuming a temperature of 400 °C and a confining pressure of 300 MPa in our field area, the estimated water fugacity is ~61 MPa.

3. Field area and sample selection

3.1. Regional geology

The SCSZ is located within the Liberty–Orrington belt of south-central Maine, USA (Fig. 3). The rocks record a complex multistage deformation history associated with the Siluro–Devonian Acadian orogeny. Deformation occurred in three major stages. Stage 1 involved the eastward subduction of the eastern margin of Laurentia underneath composite Avalon during the Late Silurian to Early Devonian. This led to the development of west-directed thrusts between ~423 and 404 Ma and may have involved recumbent folding, though the evidence is sparse (Hussey, 1988; West et al., 2021). This deformation event further developed into the regional pattern of upright, isoclinal folds pervasive in Maine's bedrock (Tucker et al., 2001; West et al., 2021). Thickening of the crust and plutonism during this time resulted in regional high-temperature, low-pressure metamorphism at upper-amphibolite facies conditions in south-central Maine (Guidotti, 1989).

Between ~399 and 380 Ma, a shift in regional kinematics from orthogonal convergence to dextral transpression coincided with the development of the Norumbega fault system (stage 2; West et al., 2003; Gerbi and West, 2007). The Norumbega fault system is defined by a ~5–40 km wide zone of heterogeneous dextral transpression (kinematic vorticity number of 0.67 recorded in calcite veins; Short and Johnson, 2006; Short et al., 2011) that occurred during or immediately following peak metamorphic conditions. Structures indicative of dextral transpression include asymmetric boudinage of quartz veins and pegmatite pods, shear banding, and the development of north-verging asymmetric z-folds with steeply dipping axial planes and shallow-to moderately-plunging fold axes (Swanson, 1992, 1999, 2006a, 2006b; West et al., 2003).

Superimposed upon this wider zone of dextral shear are several, highly localized (<2 km), high-strain dextral shear zones that define stage 3 and formed parallel to the preexisting high-temperature foliation and compositional layering associated with stages 1 + 2. The degree of localization along the Norumbega fault system varies along strike, with

Table 1
Flow laws and associated parameters used in strain rate calculations.

Source	Flow laws	A ($MPa^{-n-m}s^{-1}$)	n	Q *or* H (kJ/mol)	m	V (cm^3/mol)
Tokle et al. (2019) (low-stress, high-T)	$\dot{\varepsilon} = A\sigma^n f_{H_2O}^m \exp\left(\frac{-Q}{RT}\right)$	1.75×10^{-12}	4	125	1	N/A
Lu and Jiang (2019)	$\dot{\varepsilon} = A\sigma^n f_{H_2O}^m \exp\left(\frac{-(H+pV)}{RT}\right)$	6×10^{-15}	4	132	2.7	35.3
Lusk et al. (2021) (low-pressure)	$\dot{\varepsilon} = A\sigma^n f_{H_2O}^m \exp\left(\frac{-(H+pV)}{RT}\right)$	5.01×10^{-10}	3.5	118	0.49	2.59

Note: $\dot{\varepsilon}$ – strain rate (s^{-1}); A – preexponential factor ($MPa^{-n-m}s^{-1}$); σ – differential stress (MPa); n – stress exponent; f_{H_2O} – water fugacity (MPa); m – fugacity exponent; Q – activation energy (J/mol); H – activation enthalpy (J/mol); p – pressure (MPa); V – activation volume (cm^3/mol); R – universal gas constant (=8.314 J K^{-1}·mol^{-1}); T – absolute temperature (K).

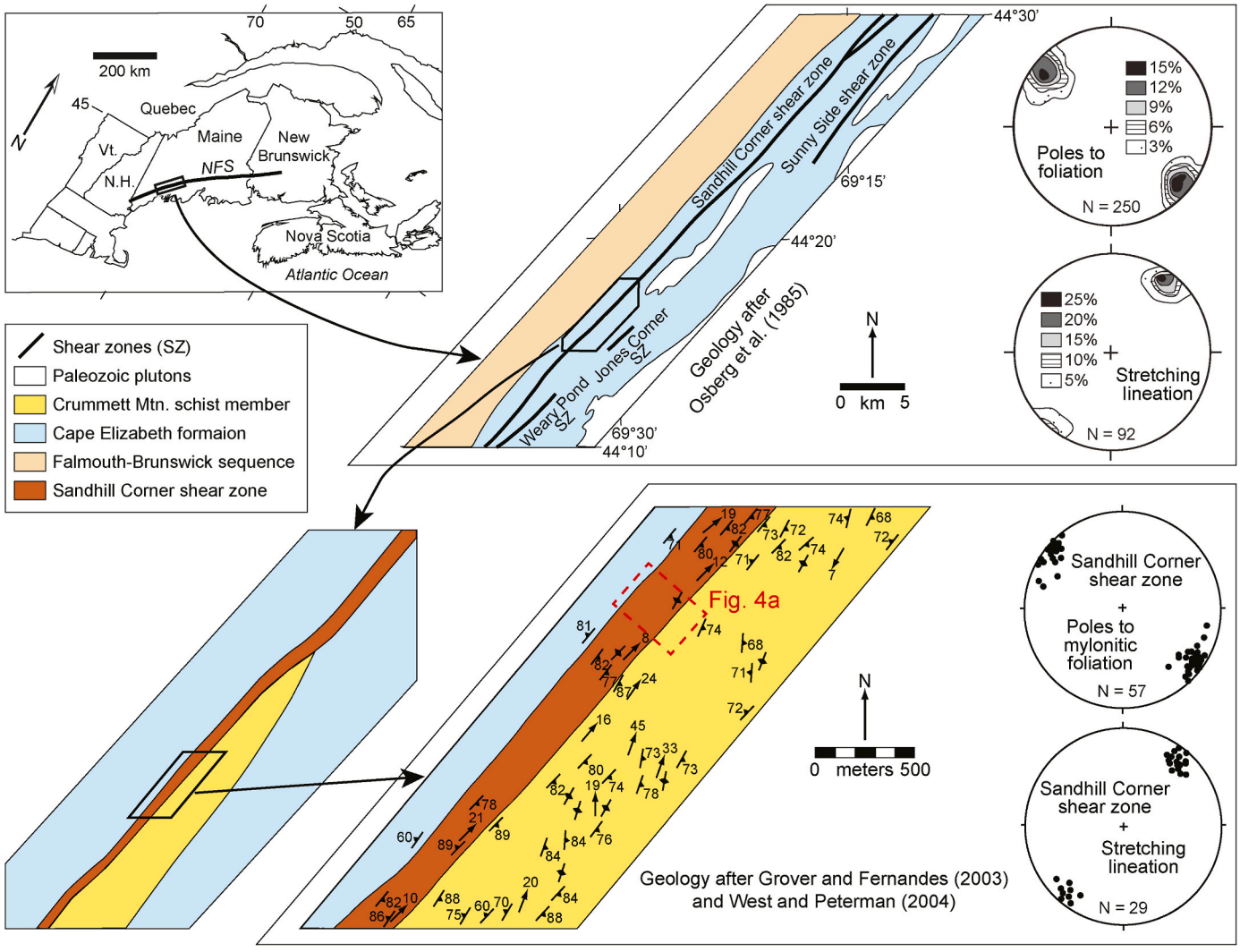

Fig. 3. Geologic map of the SCSZ and its regional context within the Norumbega fault system (NFS). Lower-hemisphere, equal-area projections in the upper right panel show poles to foliation and stretching lineation measured from rocks along the broader field area. In the lower right panel, the same projections show the mylonitic foliation and lineation associated with the SCSZ. The dashed red box in the lower right panel outlines the study area in Fig. 4a. Adapted from Johnson et al. (2009). (For interpretation of the references to colour in this figure legend, the reader is referred to the Web version of this article.)

mylonites and ultramylonites dominant to the southwest which transition to phyllonites, cataclasites, and breccias to the northeast (Hatheway, 1971; Swanson, 1992, 1999, 2006a, 2006b; West and Hubbard, 1997; Wang and Ludman, 2004; Short et al., 2011). The primary cause for the variation in structural style of localization during stage 3 is thought to result from decreasing temperatures associated with differential exhumation following stage 2, exposing deeper crustal levels to the southwest and shallower crustal levels to the northeast (Guidotti, 1989; West et al., 1993; Hubbard et al., 1995; West and Hubbard, 1997; Ludman and Gibbons, 1999; Swanson, 1999; Wang and Ludman, 2004). Because the structural expression of stage 3 varies along strike, we restrict our detailed description of this event to its expression within the SCSZ in south-central Maine.

3.2. Sandhill Corner shear zone

The SCSZ is a ~230 m wide vertical, high strain, dextral strike-slip seismogenic shear zone located within the Norumbega fault system in south-central Maine (Fig. 4a; Ludman and West, 1999). Deformation along the SCSZ is dominantly simple shear, exhibiting a kinematic vorticity number of 0.97 (Johnson et al., 2009), and is concentrated at the contact between the quartzofeldspathic (QF) unit of the Cape Elizabeth formation and the mica schist of the Crummett Mountain formation (Grover and Fernandes, 2003; West and Peterman, 2004; Price et al., 2016). The Cape Elizabeth formation is a quartz + plagioclase + biotite ± garnet ± sillimanite metasedimentary rock exhibiting partial migmatization and metamorphism at upper amphibolite-facies conditions (Grover and Fernandes, 2003; West and Peterman, 2004). The Crummett Mountain formation (equivalent to the Scarboro Formation of Grover and Fernandes, 2003) is a quartz + plagioclase + garnet + staurolite + andalusite mica schist, metamorphosed under similar conditions to the Cape Elizabeth formation and hosts discontinuous, strongly folded quartz veins. A combination of $^{40}Ar/^{39}Ar$ thermochronology and detailed microstructural studies have revealed two major episodes of dextral shear affecting the SCSZ. Stage 2 is an earlier period of >25 km wide distributed dextral shear characterized by high-temperature (≥~500 °C) deformation initiated at or immediately following a period of Middle Devonian amphibolite facies metamorphism (500–600 °C; 300–400 MPa) at ~380 Ma (West and Hubbard, 1997). Stage 3 is a later period of localized, high-strain mylonitization and sustained seismogenic deformation at depths corresponding to the frictional-to-viscous transition (~400–500 °C). The timing of stage 3 is bracketed by an initial release $^{40}Ar/^{39}Ar$ cooling age of ~290 Ma on the recrystallized margin of muscovite porphyroclasts within the SCSZ, indicating ~100 Ma of activity along the shear zone (West and Lux, 1993). Whether this long-lived period of deformation was continuous or punctuated is an open question.

Evidence for viscous strain localization along the contact between the Cape Elizabeth and Crummett Mountain formations occurs in the form of marked grain size reduction in quartz grains within both pure quartz veins and quartz-rich selvages within felsic layers, an increase in aspect ratio of these quartz domains, a decrease in the proportion of

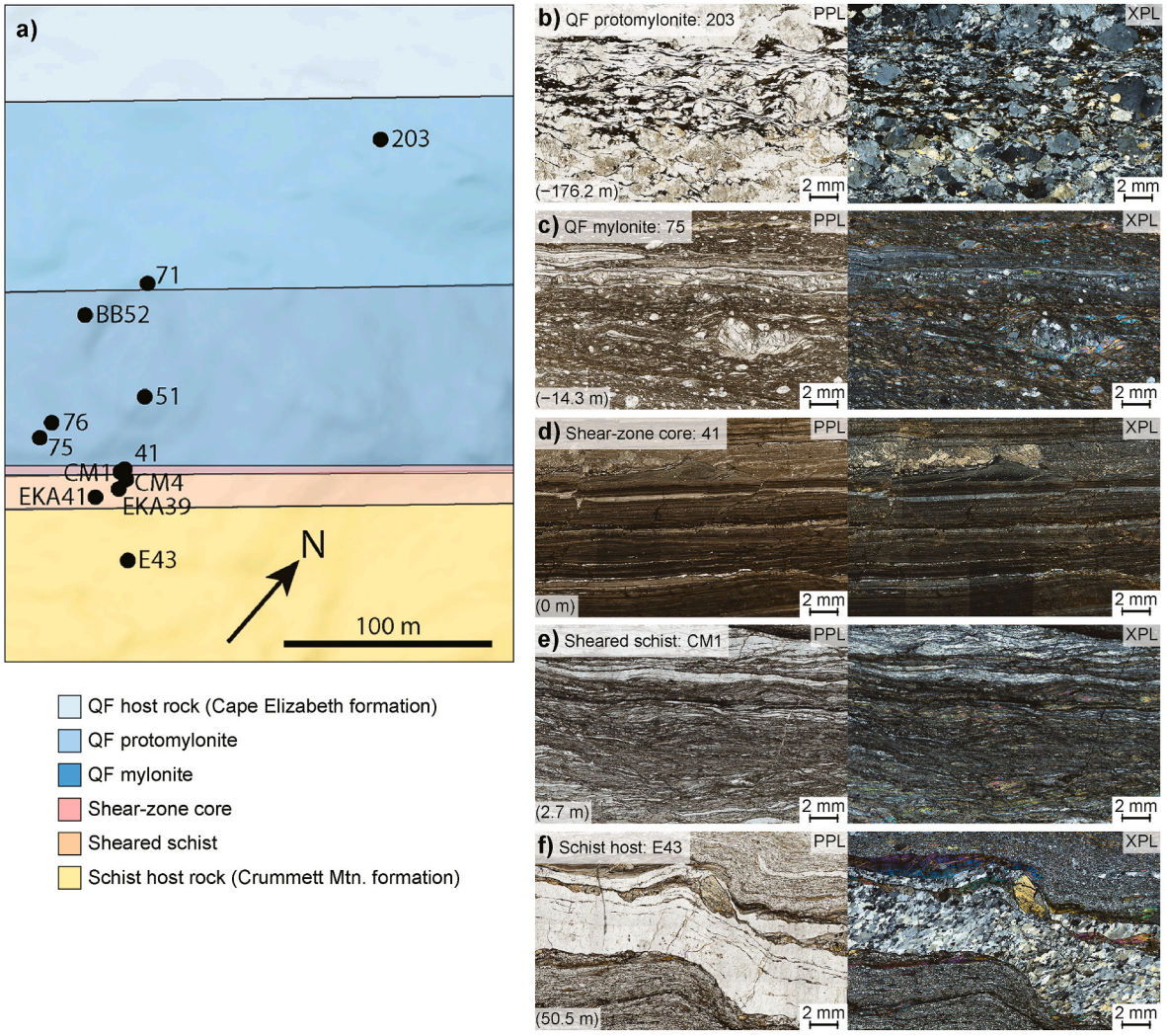

Fig. 4. Sample location and general rock microstructures. (a) Hillshade basemap of the study area with sample locations and rock types overlain for reference. QF – quartzofeldspathic. (b–f) Photomicrographs demonstrating broad structural characteristics of strain localization along the SCSZ. The distance from the shear-zone core is displayed in the lower left of each panel. (b) QF protomylonite shows the development of anastomosing shear bands of mica and oxides and quartz-rich domains wrapping around rigid feldspar porphyroclasts. (c) QF mylonite shows strain localization accompanied by marked grain size reduction of porphyroclasts of feldspar, mica fish, and matrix minerals. (d) Ultramylonitic shear-zone core sample showing a relatively young pseudotachylyte layer exhibiting flow banding (top). See Fig. 5d for quartz microstructures within the sample. (e) Sheared schist sample with thin, embedded quartz veins. (f) Schist host rock of the Crummett Mountain formation with a thick embedded quartz vein. The marked reduction in grain size and vein thickness outlines the viscous strain gradient. PPL – plane-polarized light; XPL – cross-polarized light.

feldspar porphyroclasts and mica fish relative to the matrix, and an increase in mica content toward the shear-zone core, particularly within the Cape Elizabeth formation (Fig. 4b–f). The thickness of pure quartz domains also decreases with increasing proximity to the shear-zone core within both rock types (Anderson, 2017; W.J. Song et al., 2020b), which allowed strain gradient measurements. The viscous strain gradient is asymmetrically distributed around the core of the shear zone and varies in width along strike. Within the QF unit, a zone of protomylonite extends from ~200 m to ~90 m away from the shear-zone core. The protomylonite transitions into a mylonite zone within ~90 m of the core and effectively becomes fully recrystallized within the innermost ~40 m. The shear-zone core consists of a ~5 m-wide ultramylonite/phyllonite that forms a topographic trough in the field area. In the schist unit, a region of highly sheared schist can be found up to ~20 m from the core, beyond which strain is heterogeneously distributed. Viscous strain localization likely occurred during regional cooling during exhumation, as evident by the change in dominant quartz deformation mechanism from high-temperature grain boundary migration (GBM) recrystallization to lower-temperature subgrain rotation recrystallization (SGR; see Section 3.3 for details on quartz microstructures).

The stage 3 structure of the SCSZ is delimited not only by the development of a viscous strain gradient but contains structures indicative of sustained seismogenic deformation at the frictional-to-viscous transition zone. Such structures include the occurrence of mutually overprinting pseudotachylyte and mylonite (Price et al., 2012), the occurrence of dynamically fragmented garnets which have subsequently

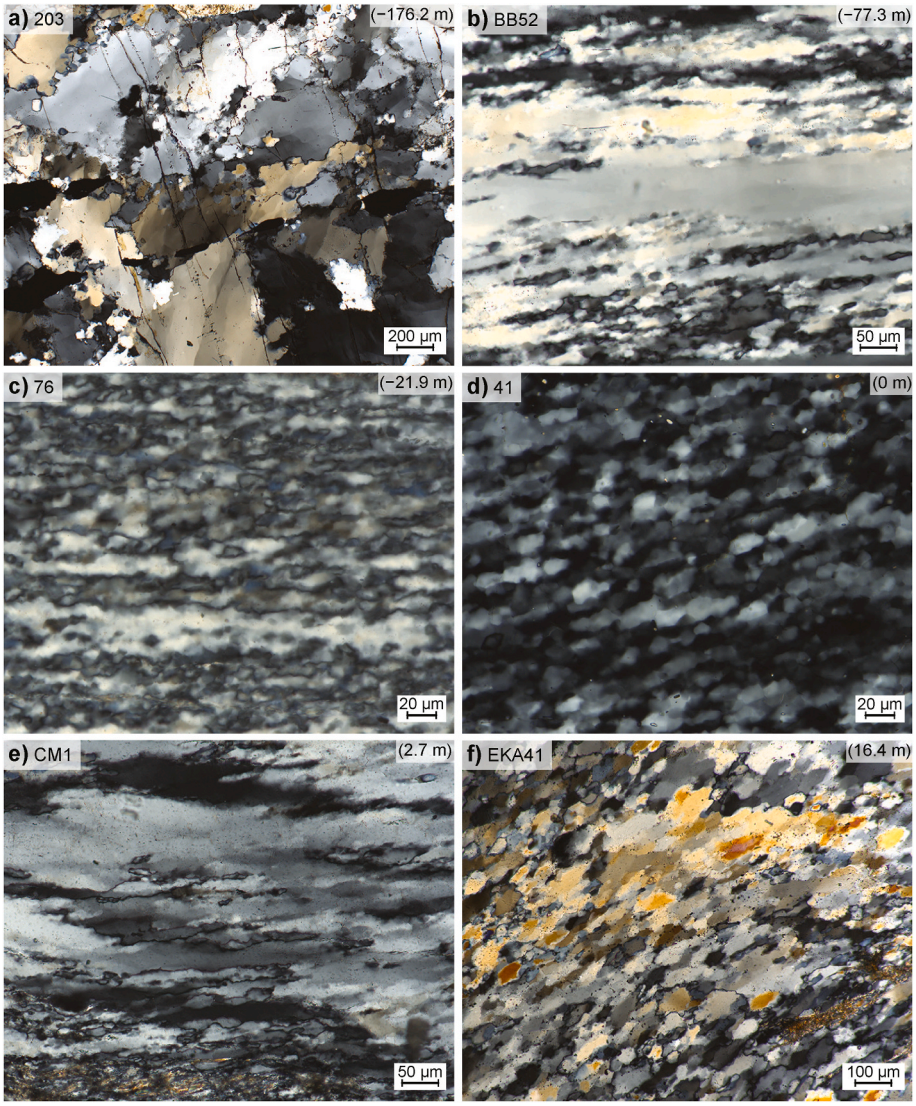

Fig. 5. Photomicrographs in cross-polarized light demonstrating the nature of quartz microstructures across the SCSZ. Sample name and distance from the shear-zone core are listed in the upper left and right corners of each photomicrograph, respectively. Note that photomicrographs were taken at various scales. (a) Large, relict, amoeboid quartz grains exhibiting intracrystalline lattice distortion and formation of subgrains and recrystallized grains along their margins. (b) Highly elongate relict grains exhibiting subgrain nucleation both along their margins and in the interior of the relict grains. Recrystallized grains show progressive misorientation from the relict grain interiors to their margin, indicative of recrystallization via subgrain rotation recrystallization. (c) Quartz vein in the inner mylonite zone demonstrating effectively complete recrystallization via subgrain rotation recrystallization. (d) Recrystallized quartz grains within the shear-zone core. Note that while quartz grains within the core are similar in size to those within the inner mylonite, they exhibit less irregular grain boundaries, less lattice distortion, and some triple junctions along subgrain/grain boundaries. (e) A quartz vein within ~5 m of the shear-zone core in the sheared schist. Quartz grains resemble those of the outer mylonite, with highly elongate relict grains grading to subgrains and recrystallized grains progressively along their margins. Unlike quartz veins within the inner mylonite, those in the sheared schist of the Crummett Mountain formation do not exhibit complete recrystallization. (f) Quartz microstructures in the outer portions of the sheared schist, demonstrating similar microstructures to those in the protomylonite. Samples are cut perpendicular to foliation and parallel to the stretching lineation and exhibit a dextral sense of shear from quartz shape-preferred orientations.

been stretched and elongated due to viscous flow in the interseismic period (B.R. Song et al., 2020a), dynamically kinked mica fish (Anderson et al., 2021), and fluid inclusion amount patterns recorded in quartz veins representing coseismic fluid infiltration and removal via dynamic recrystallization during the coseismic and post-/interseismic periods, respectively (W.J. Song et al., 2020b). The abundance of recrystallized/devitrified pseudotachylyte in thin section exhibits local variation but tends to increase within ~35 m of the shear-zone core in the Cape Elizabeth formation from ~10 to 30 % to ~40–70 % within the core (W.J. Song et al., 2020b). These observations of coseismic damage within the mylonite zone led to further classification of the mylonite into inner (<~35 m) and outer (~35–90 m) zones relative to the shear-zone core. In the Crummett Mountain formation, the occurrence of dynamically fragmented garnets within ~5 m of the core allows another classification of the sheared schist into inner (<~5 m) and outer (~5–27 m) zones. Thus, four samples 76, 75, 41 and CM1 (Fig. 4a) are considered as the inner shear zone samples affected by coseismic damage.

3.3. Quartz microstructures and deformation temperature estimates

Quartz veins within the field area contain microstructures reflecting the multistage deformation history outlined above. High temperature GBM recrystallization associated with stage 2 produced large, amoeboidal quartz grains within quartz veins and quartz rich selvages in both host rocks. These higher temperature microstructures are overprinted by those indicative of lower temperature deformation within the SGR field and are associated with stage 3. Fig. 5 shows photomicrographs illustrating the change in the degree of quartz recrystallization across the SCSZ. Within the protomylonite, large, relict, amoeboid quartz grains begin to show marked intracrystalline lattice distortion and formation of subgrains along their margins, with recrystallized grains forming along the grain boundaries of the relict grains (Fig. 5a). Within the outer mylonite zone, relict grains are highly elongated and exhibit subgrain nucleation both along their margins and in the interior of the relict grains (Fig. 5b). Recrystallized grains show progressive misorientation from the relict grain interiors to their margin, indicative of recrystallization via SGR. Within the inner mylonite zone, quartz veins are effectively fully recrystallized (Fig. 5c). Widespread lattice distortion is observed in recrystallized grains accompanied by subgrain formation. The grain boundaries of recrystallized grains are irregular. Recrystallized quartz grains within the shear-zone core (Fig. 5d) are similar in size to those within the inner mylonite, but exhibit less irregular grain boundaries, less lattice distortion, and some triple junctions observed along subgrain/grain boundaries. Within ~5 m of the core in the sheared schist, quartz grains resemble those of the outer mylonite, with highly elongated relict grains transitioning to subgrains and recrystallized grains progressively along their margins (Fig. 5e). Unlike quartz veins within the inner mylonite, those in the sheared schist of the Crummett Mountain formation do not exhibit complete recrystallization. In the outer portions of the sheared schist, microstructures are similar to those in the protomylonite, with larger relict grains exhibiting internal lattice distortions and subgrain formation with recrystallized grains forming along their margins (Fig. 5f).

The observation of SGR microstructures along the SCSZ during stage 3 suggests deformation temperatures in the range of ~400–500 °C (Stipp et al., 2002). Additional temperature constraints can be estimated using the opening angle of quartz c-axis fabric pole figures (e.g., Law, 2014; Faleiros et al., 2016). Using the low-temperature equation of Faleiros et al. (2016), opening angle estimates from EBSD data collected from five quartz vein samples used in Price et al. (2016) yield average deformation temperatures across the shear zone of ~411 ± 32 °C (Fig. S1). For the purposes of this paper, we assume a deformation temperature of 400 °C.

3.4. Sample selection and grain boundary tracing

To assess the GBD method, it is important to apply it to monomineralic quartz aggregates and use photomicrographs in cross-polarized light taken with multiple polarizer orientations to accurately identify recrystallized quartz grain boundaries. Eleven samples within the SCSZ were selected (Fig. 4a). Five samples in the Cape Elizabeth formation are the doubly polished thin sections used in W.J. Song et al. (2020b). All samples were cut perpendicular to the local foliation and parallel to the local stretching lineation. Thin sections of ~30 μm thickness were prepared to observe microstructures and trace grain boundaries of recrystallized quartz. Optical micrographs (with cross-polarized light) of monomineralic quartz aggregates were taken using the × 10–20 objective lens in a polarized light microscope. Regions of monomineralic polycrystalline quartz were selected to ensure that grain boundary kinetics were not influenced by secondary phases. In each sample, we imaged the same field of view using 5–9 varying orientations of the polarizers (typically at 10° intervals) for precise discrimination of subgrain and grain boundaries. We used a tablet computer with a stylus pen to draw grain boundaries on the photomicrograph. Confident selection of recrystallized quartz grains can be difficult using optical methods because relict grains also could be of similar size owing to 2D cutting effects. In the samples with fully recrystallized quartz (samples 76, 75 and 41) within the innermost ~35 m of the QF unit including the ultramylonite, any grains with clearly displayed boundaries can be selected (Fig. 6a). In the QF mylonite samples with partially recrystallized quartz (sample BB52 and 51), the quartz aggregates show highly elongated large relict quartz with long axes parallel to the foliation, surrounded by relatively fine-grained recrystallized quartz. We chose such recrystallized grains in the QF mylonites (Fig. 6b). However, in the QF protomylonite (samples 203 and 71) and sheared schist samples with partially recrystallized quartz aggregates (samples CM1, CM4, EKA39 and EKA41), we could not confidently identify recrystallized grains optically because the grain size distributions of relict and recrystallized quartz overlap. We resolved this with the aid of electron backscattered diffraction (EBSD), separating relict and recrystallized grains using a threshold value of grain orientation spread in the same way as Cross et al. (2017) (Fig. 6c; see the supplementary material and Fig. S2 for EBSD setup and postprocessing). Note that even for those grains identified as recrystallized via EBSD, we use the optical measurements of the grain boundaries in our analysis, as the EBSD data were collected at too coarse a resolution to accurately identify grain perimeters. Moreover, the GBD method was originally developed using optical microscopy (Takahashi et al., 1998). In this study, 50–138 recrystallized grains were measured per sample. The traced grain boundaries of the recrystallized quartz were used in ImageJ software to compute perimeter, area, and aspect ratio of the fitted ellipse for each grain. The average 2D grain size of the recrystallized quartz was calculated as the root-mean-square diameter.

4. Results

4.1. D-value variation across the Sandhill Corner shear zone

To examine the dependence of D-value on the number of measured grains in a sample, a sensitivity analysis was conducted to observe the change in D-value and standard error associated with the number of measured grains that are randomly chosen. The sensitivity analyses show that above ~30–40 measurements, the D-value and associated standard error stabilize, and additional measurements reduce the standard error (Fig. S3). This observation suggests that our results for each sample are based on a large enough number of grains to be reliable. The number of measured grains in each sample is listed in Table 2.

The perimeter and diameter measurements of recrystallized quartz grains show strong power-law relationships for all samples (R^2 ranges between 0.96 and 0.98; see Fig. S4). Calculated D-values vary across the

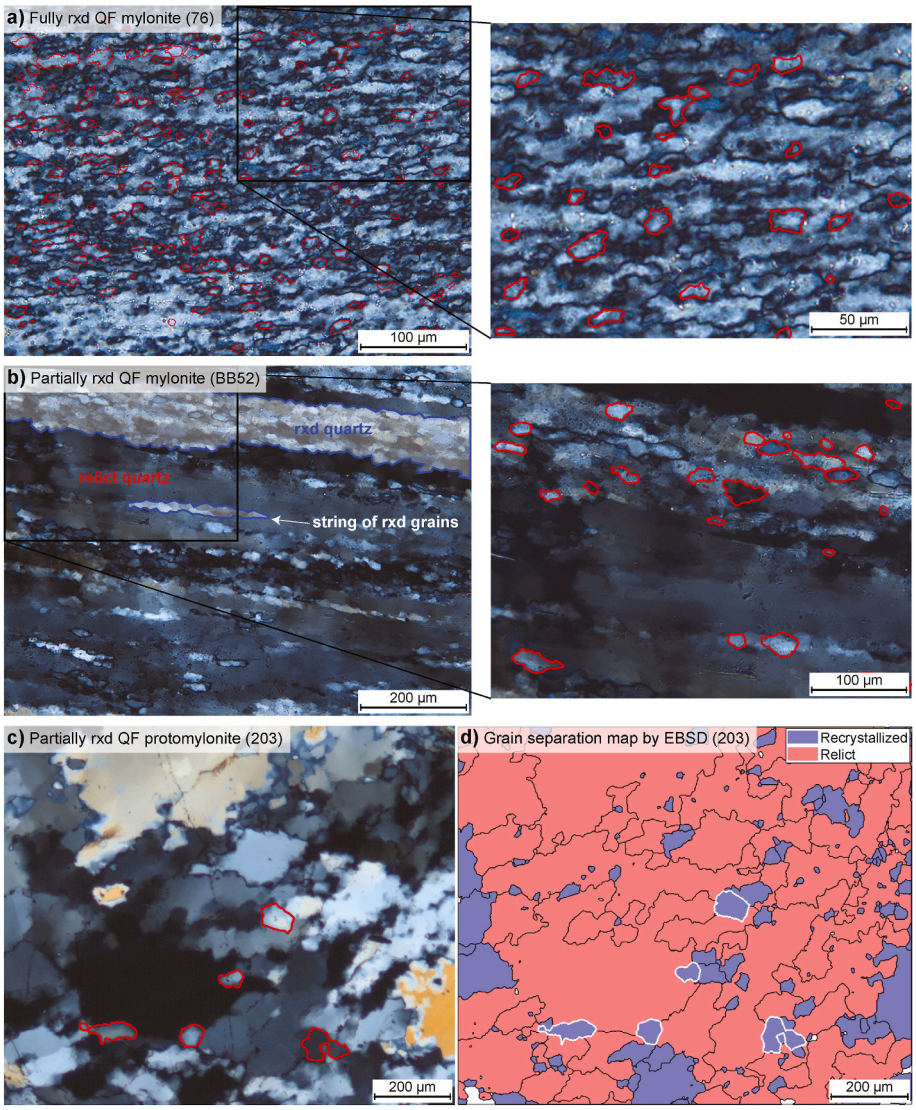

Fig. 6. Examples of tracing grain boundaries of recrystallized (rxd) quartz marked by red lines in the photomicrographs. The traced grain boundaries are from multiple photomicrographs with varying orientations of the polarizers to see clear grain boundaries. (a) Fully recrystallized quartzofeldspathic (QF) mylonite (sample 76). (b) Partially recrystallized QF mylonite (sample BB52). Note clear recognition of relict and recrystallized quartz. (c) Partially recrystallized QF protomylonite (sample 203). Recrystallized quartz was identified by the aid of EBSD grain separation map. (d) Grain separation map between relict and recrystallized quartz by EBSD (sample 203). This map was generated in the same way as Cross et al. (2017). White lines mark the same grains traced in the photomicrograph of (c). Photomicrographs are taken by cross-polarized light. (For interpretation of the references to colour in this figure legend, the reader is referred to the Web version of this article.)

SCSZ (Table 2; Fig. 7; for analyzed raw data set of individual samples, see the Excel file of the supplementary material). D-values in the QF protomylonite are relatively constant at ~1.05. Within the QF mylonite, D-values increase to ~1.2 at ~40 m from the shear-zone core before decreasing back down to values as low as ~1.1 at the core. This decreasing trend continues into the sheared schist, where D-values are constant within error at ~1.07. The observed decrease in D-values within ~40 m of the core in the QF mylonite coincides well with the occurrence of coseismic indicators described in Section 3.2.

4.2. Strain-rate variation across the Sandhill Corner shear zone

Flow stresses and strain rates calculated in this study are listed in Table 3. Away from the shear-zone core, strain rates derived from D-values and a temperature of 400 °C are on the order of $10^{-10.7–11.2}$ s^{-1} (Fig. 8). Within the QF mylonite, strain rates increase to ~$10^{-9.4}$ s^{-1}, decreasing gradually within ~40 m of the core to values around ~$10^{-10.3}$ s^{-1}. Strain rates within the sheared schist are rather uniform around ~$10^{-10.6}$ s^{-1}. These strain rates are ~1.5–3.5 orders of magnitude faster than those predicted by the comparative flow laws using the piezometer of Stipp and Tullis (2003) (Fig. 8a). The experimental flow law of Lu and Jiang (2019) represents the lower limit, with the naturally constrained low-stress flow law of Tokle et al. (2019) predicting intermediate values. The low-pressure flow law of Lusk et al. (2021) predicts the fastest strain rates out of the three flow laws, yet still lying ~1.5 orders of magnitude slower than those predicted by D-values. Application of the temperature-dependent piezometer of Shimizu (2012) shifts the flow laws of Tokle et al. (2019), Lu and Jiang (2019), and Lusk et al. (2021) to faster strain rates by ~1.5 orders of magnitude, causing strain rates calculated from the flow law of Lusk et al. (2021) to lie within half an order of magnitude of those calculated from D-values (Fig. 8b). Despite the variation in strain-rate magnitude between methods, the spatial pattern of flow law-derived strain rates is very similar to the spatial pattern of strain rates derived from D-values except for the inner shear zone samples (see Fig. S5).

Table 2
Calculated D-values, recrystallized grain sizes, and shape properties from samples across the SCSZ. Italicized samples (76, 75, 41 and CM1) are those lying within the coseismic damage zone (inner shear zone).

Sample	Latitude	Longitude	Rock type	Distance (m)	D-value	Average grain size (μm)	Average aspect ratio	Average circularity	Average roundness	$\overline{P}_{norm}$	*N*
203	44.2736288	−69.5051955	QF proto-mylonite	−176.2	1.06 ± 0.03	38.1 ± 13.6	1.60 ± 0.31	0.66 ± 0.10	0.73 ± 0.09	1.19	50
71	44.2723763	−69.5054353	QF proto-mylonite	−96.1	1.02 ± 0.02	45.8 ± 18.6	1.63 ± 0.47	0.66 ± 0.08	0.74 ± 0.08	1.17	50
BB52	44.2720608	−69.5055204	QF mylonite	−77.3	1.15 ± 0.02	18.5 ± 6.7	1.96 ± 0.55	0.69 ± 0.11	0.82 ± 0.05	1.10	50
51	44.2720456	−69.5048812	QF mylonite	−38.6	1.19 ± 0.03	11.1 ± 5.0	2.24 ± 0.76	0.65 ± 0.14	0.83 ± 0.07	1.09	50
76	*44.2716395*	*−69.5051158*	*QF mylonite*	*−21.9*	*1.18 ± 0.02*	*10.6 ± 3.9*	*1.88 ± 0.62*	*0.65 ± 0.13*	*0.77 ± 0.09*	*1.16*	*138*
75	*44.2716395*	*−69.5051158*	*QF mylonite*	*−14.3*	*1.17 ± 0.03*	*10.0 ± 3.0*	*1.89 ± 0.65*	*0.68 ± 0.12*	*0.80 ± 0.08*	*1.12*	*99*
41	*44.2715585*	*−69.5050900*	*Core*	*0*	*1.11 ± 0.02*	*12.4 ± 5.0*	*1.90 ± 0.51*	*0.67 ± 0.10*	*0.79 ± 0.05*	*1.13*	*50*
CM1	*44.2717426*	*−69.5045838*	*Sheared schist*	*2.7*	*1.11 ± 0.03*	*11.1 ± 4.4*	*1.99 ± 0.61*	*0.68 ± 0.10*	*0.82 ± 0.06*	*1.10*	*50*
CM4	44.2717325	−69.5045446	Sheared schist	6.4	1.07 ± 0.02	31.5 ± 13.2	1.78 ± 0.49	0.65 ± 0.10	0.76 ± 0.08	1.17	50
EKA39	44.2716871	−69.5045273	Sheared schist	9.5	1.08 ± 0.02	26.5 ± 11.0	1.82 ± 0.38	0.67 ± 0.10	0.78 ± 0.07	1.14	50
EKA41	44.2715789	−69.5045639	Sheared schist	16.4	1.07 ± 0.02	32.6 ± 10.9	1.64 ± 0.41	0.72 ± 0.09	0.80 ± 0.06	1.12	50

Note that the average grain size represents the root-mean-square of all recrystallized grains in the sample, whereas other averages are conducted using the arithmetic mean. $\overline{P}_{norm}$ – average normalized ellipse perimeter; *N* – number of measured grains. Errors of D-value are 1 standard error, and the other properties of grain size, aspect ratio, circularity and roundness show 1 standard deviation. See the Excel file of the supplementary material for the raw data of Table 2.

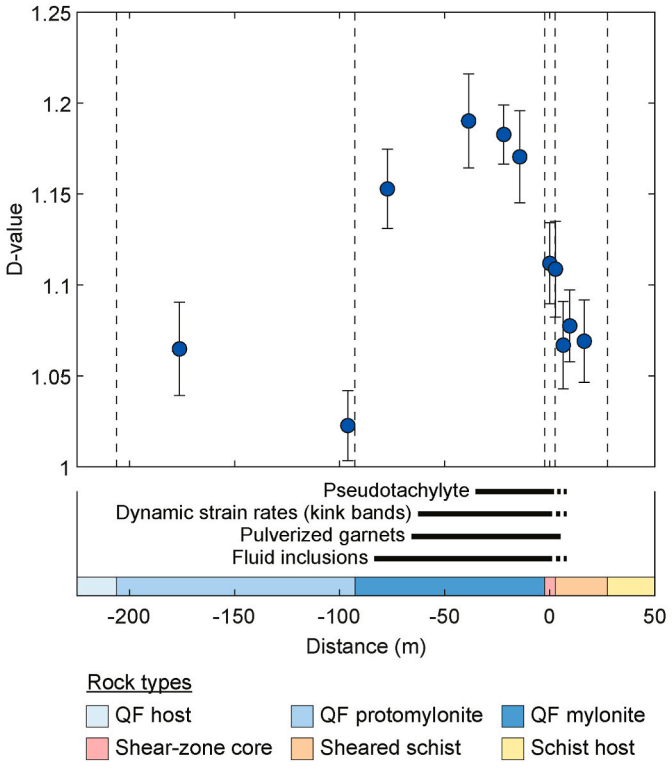

Fig. 7. The spatial variation in measured D-value from samples across the SCSZ. The spatial extent of structures indicative of coseismic damage and associated structural zones are shown below for reference. High D-values are found in the QF mylonite, but D-values decrease toward the shear-zone core within the innermost ~40 m of the QF mylonite and ~5 m of the sheared schist, which coincide with the occurrence of coseismic indicators.

4.3. Comparison of D-values and shape properties

Shape property calculations are listed in Table 2. To explore correlations between D-values and common indicators of grain shape and form, we plot the variation in D-value as a function of average grain size, average aspect ratio, average circularity, average roundness, and average normalized ellipse perimeter $\overline{P}_{norm}$ (Fig. 9). Linear best-fit lines were obtained using the Curve Fitting toolbox in MATLAB v2023a. We report the R^2 value to qualitatively discuss any degree of correlation between variables. D-values display a strong negative correlation with average grain size, a strong positive correlation with average aspect ratio, no correlation with average circularity, a moderate positive correlation with average roundness, and a weak negative correlation with $\overline{P}_{norm}$. Fig. 9f demonstrates that the average roundness and $\overline{P}_{norm}$ are inversely correlated with one another and both are reliable indicators of surface roughness.

5. Discussion

5.1. Relationship between D-value and grain size

Both methods employed in this study for calculating strain rates were calibrated for monomineralic quartz aggregates deformed in the dislocation creep regime. Due to widespread evidence of transient coseismic damage concentrated within the inner mylonite zone and immediately adjacent to the shear-zone core within the sheared schist, we expect that samples located within this zone likely contain disequilibrium microstructures that involve contributions from both dislocation creep and grain-size sensitive creep. We filter these samples out when evaluating the relationship between D-values, shape properties, and strain-rate estimates, but explore their significance near the shear-zone core later in the discussion. The four filtered samples (three QF mylonites and one sheared schist) that lie within this zone of transient coseismic deformation are outlined by red boundaries in Figs. 8–10.

Upon filtering the data, the reduced dataset exhibits a strong negative correlation between D-value and recrystallized grain size. Similar

Table 3
Flow stresses and $\log_{10}$ strain rates calculated from recrystallized grain sizes, D-values, and flow laws. Italicized samples (76, 75, 41 and CM1) are those lying within the coseismic damage zone (inner shear zone).

Sample	Flow stress (MPa)[a]		$\log_{10}$ strain rate (s^{-1})[b]						
	Stipp and Tullis (2003)	Shimizu (2012)	D-value	Tokle et al. (2019)		Lu and Jiang (2019)		Lusk et al. (2021)	
203	37.7	80.3	−10.7	−13.4	(−12.1)	−14.2	(−12.9)	−12.1	(−11.0)
71	32.6	69.3	−11.2	−13.6	(−12.3)	−14.4	(−13.1)	−12.3	(−11.2)
BB52	66.9	143.4	−9.8	−12.4	(−11.0)	−13.2	(−11.8)	−11.3	(−10.1)
51	96.0	206.9	−9.4	−11.7	(−10.4)	−12.5	(−11.2)	−10.7	(−9.5)
76	*103.8*	*223.8*	*−9.5*	*−11.6*	*(−10.3)*	*−12.4*	*(−11.1)*	*−10.6*	*(−9.4)*
75	*108.8*	*234.7*	*−9.6*	*−11.5*	*(−10.2)*	*−12.3*	*(−11.0)*	*−10.5*	*(−9.3)*
41	*91.4*	*196.8*	*−10.2*	*−11.8*	*(−10.5)*	*−12.6*	*(−11.3)*	*−10.8*	*(−9.6)*
CM1	*99.7*	*214.9*	*−10.3*	*−11.7*	*(−10.3)*	*−12.5*	*(−11.1)*	*−10.6*	*(−9.5)*
CM4	43.8	93.5	−10.7	−13.1	(−11.8)	−13.9	(−12.6)	−11.9	(−10.7)
EKA39	50.3	107.4	−10.6	−12.9	(−11.6)	−13.7	(−12.3)	−11.7	(−10.5)
EKA41	42.7	91.0	−10.7	−13.2	(−11.8)	−14.0	(−12.6)	−11.9	(−10.8)

[a] Flow stress of each sample is calculated by two piezometers of Eq. (2a) for Stipp and Tullis (2003) and Eq. (2b) for Shimizu (2012). The average grain size in Table 2 and a temperature of 400 °C are used for the calculation.

[b] D-value-based strain rates are estimated by Eq. (1) and the D-values in Table 2; flow law-based strain rates are estimated by the equations and parameters in Table 1, assuming a temperature of 400 °C and a confining pressure of 300 MPa. Two piezometers of Stipp and Tullis (2003) and Shimizu (2012) are used in calculating the differential stress of three flow laws. Strain rates using Shimizu (2012) are shown in parentheses. See the Excel file of the supplementary material for the raw data of Table 3.

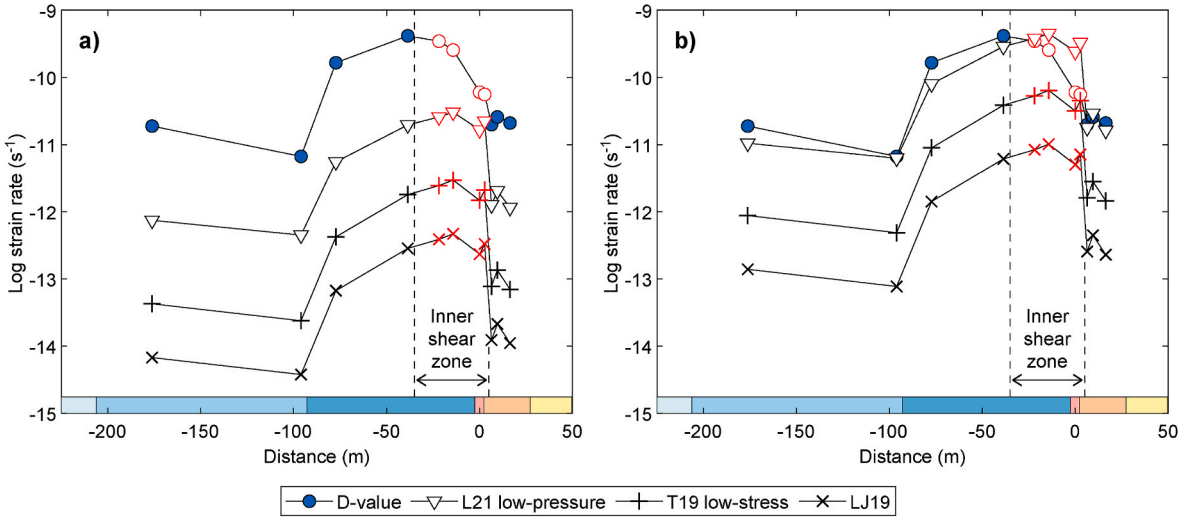

Fig. 8. Strain rate calculations from measured D-values (blue circles) and flow laws combined with two different grain size piezometers: (a) Stipp and Tullis (2003)'s piezometer and (b) Shimizu (2012)'s temperature dependent piezometer. L21 – low-pressure flow law of Lusk et al. (2021); T19 – low-stress flow law of Tokle et al. (2019); LJ19 – Lu and Jiang (2019). The data points with red borders indicate the four samples within the inner shear zone that sustained significant coseismic damage. The spatial pattern of flow law-based strain rates is very similar to that of D-value-based strain rates except for the four inner shear zone samples. See Fig. S5 for difference plot between D-value-based and flow law-based strain rates. (For interpretation of the references to colour in this figure legend, the reader is referred to the Web version of this article.)

relationships are observed in deformation experiments on metals (e.g., Fig. 1b and c; Z. Wang et al., 2010). Deformation experiments and theory also predict a correlation between recrystallized grain size and flow stress of quartz aggregates undergoing dislocation creep (e.g., Stipp and Tullis, 2003; Shimizu, 2008, 2011 and references therein). This observation suggests that the D-value is proportional in part to the flow stress (Fig. 10a).

Examining the spatial pattern of D-values and recrystallized grain sizes across the SCSZ demonstrates that while the two properties mirror each other across the majority of the shear zone, this pattern breaks down within the inner shear zone where average grain sizes remain relatively constant while D-values decrease (Fig. 10b). This suggests that the two methods of characterizing the microstructure preserve different information. While grain size is a measure of the equivalent diameter of grains within the aggregate, the D-value depends on both the diameter (internal strain energy) and the perimeter (surface energy) of grains within the aggregate. The breakdown in perimeter-diameter scaling relationships within the inner shear zone is also observed in Fig. 9b and d, where the correlation between D-value and average aspect ratio and roundness becomes better constrained upon filtering the dataset. The spatial pattern of strain-rate estimates between D-values and flow laws combined with grain size piezometry additionally deviates within the inner shear zone (see Fig. S5). This suggests that the D-value may be sensitive to transient changes in deformation conditions that grain size alone does not record.

5.2. *Influence of transient coseismic processes on D-value*

The decrease in D-values with near-uniform grain sizes suggests that some combination of processes associated with the seismic cycle is modifying the topology of grain boundaries without obviously affecting the average grain size. Below, we propose two possible scenarios that could lead to such a pattern across the shear zone: 1) changes in the dominant deformation mechanism and 2) decreasing flow stresses

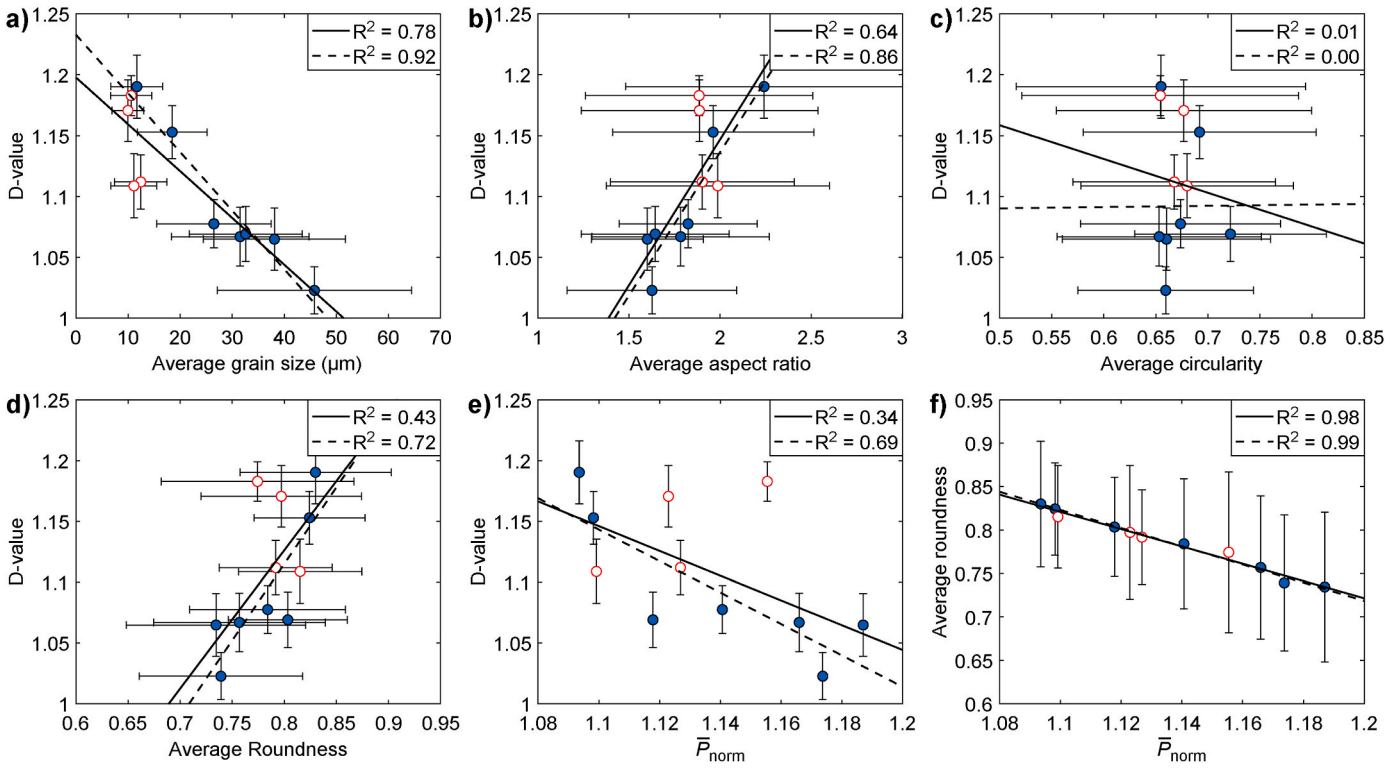

Fig. 9. Plots demonstrating the variation in D-value as a function of (a) average grain size, (b) average aspect ratio, (c) average circularity, (d) average roundness and (e) average normalized ellipse perimeter ($\overline{P}_{norm}$), and (f) the inverse relationship between average roundness and $\overline{P}_{norm}$. The linear best-fit lines and associated R^2 values for the full dataset of eleven samples and filtered data set of seven samples are shown in solid and dashed black lines, respectively. Error bars represent the standard error associated with D-values and one standard deviation for the other properties. Red data points are samples located within the inner shear zone, excluded from the filtered data set. See text for discussion. (For interpretation of the references to colour in this figure legend, the reader is referred to the Web version of this article.)

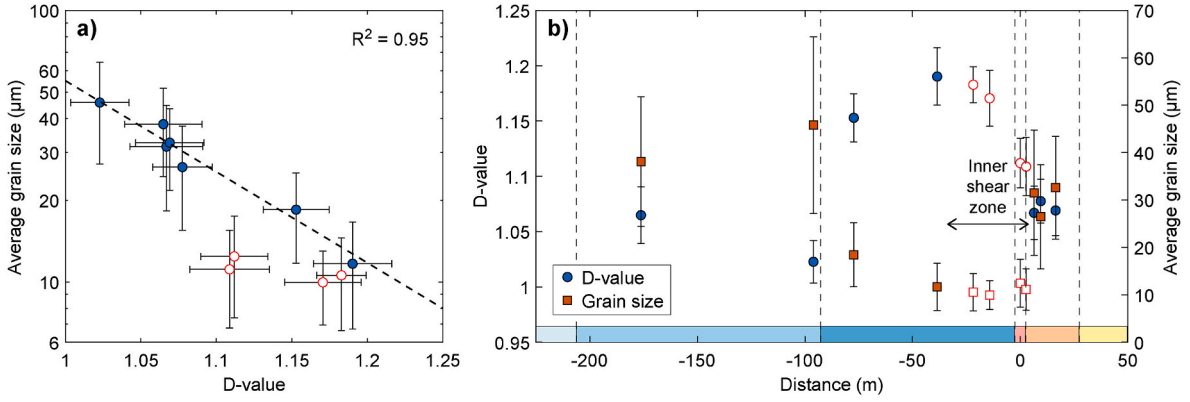

Fig. 10. (a) Plot of average grain size versus D-value in semi-log space. This relationship is similar to that of grain size piezometers. The exponential best-fit and associated R^2 value are shown for filtered data set of seven samples, except for the inner shear zone samples (red circles). (b) Spatial variation in D-value (blue circles) and average grain size (orange squares) across the SCSZ. Note that grain sizes stay relatively uniform within the inner shear zone (red open squares), whereas D-values decrease (red open circles). See text for discussion. (For interpretation of the references to colour in this figure legend, the reader is referred to the Web version of this article.)

following a coseismic rupture event. While post-tectonic grain growth/boundary modification would additionally be expected to result in decreasing D-values, we have found little evidence of such growth/annealing within samples across the SCSZ. Internal lattice distortions are common in recrystallized quartz grains, and we have observed the onset of patchy polygonization in only one sample 41 located in the shear-zone core (Fig. 5d; discussed below).

The decrease in D-value across the inner mylonite zone could reflect a change in the relative importance of deformation mechanisms. Crystallographic-preferred orientation analyses of quartz veins across the SCSZ show the development of a cross-girdle c-axis pattern in the Cape Elizabeth formation that becomes more diffuse within ~40 m from the shear-zone core (Price et al., 2016). Additionally, they reported misorientation profiles that were inconsistent with dominant SGR recrystallization. Microstructural analyses of fluid inclusions within quartz veins across the SCSZ support the interpretation that coseismic fracturing, fluid infiltration, healing, and subsequent recrystallization produced seams of fine-grained quartz aggregates and was likely a

ubiquitous process within the inner mylonite zone (W.J. Song et al., 2020b). These observations suggest that quartz aggregates within the inner mylonite zone were deforming not solely by dislocation creep, but by some combination of grain-size sensitive and insensitive creep or even proposed mechanisms such as dynamic recrystallization creep (Goldsby and Kohlstedt, 2001; Platt and Behr, 2011; Fukuda et al., 2018). Changes in deformation mechanism additionally affect the relationship between D-value and shape properties otherwise expected for dominant dislocation creep, as is shown by the improved fit upon filtering our data (dashed vs. solid fit lines in Fig. 9).

Similar arguments for a change in the proportion of dominant deformation mechanisms can be argued from the proposed relationship between the D-value and the Zener-Holloman parameter (Z). Takahashi et al. (1998) suggested that $D - 1 \propto \ln Z$, where:

$$Z = \dot{\varepsilon} \exp\left(\frac{Q}{RT}\right) \tag{6}$$

As pointed out in Takahashi et al. (1998) and Nagahama (1994), "the Zener-Hollomon parameter at constant stress deformation depends on the stress sensitivity exponent n and on the fractal dimension of the grain shape". Therefore, changes in the D-value at constant stress could indicate changes in the value of the stress exponent which is known to reflect changes in deformation mechanism (e.g., Fukuda et al., 2018). Deformation experiments on quartzite cataclasite meant to simulate deformation at the frictional-to-viscous transition zone demonstrate a stress exponent that is lower than that predicted for pure dislocation creep (Richter et al., 2018). Since grain-size sensitive creep has a stress exponent of unity, mixtures of dislocation creep and grain-size sensitive creep are likely to result in a lower bulk stress exponent than predicted from pure dislocation creep alone. If stress was nearly constant across the inner mylonite zone as suggested by average grain size, then a decrease in stress exponent in this zone due to mixed deformation mechanisms would result in a decrease in D-value at constant stress. We suggest that the D-value may therefore record variations in the relative proportions of deformation mechanisms operating within a dynamically recrystallizing monomineralic aggregate.

Alternatively, the decreasing D-values near the shear-zone core may reflect decreasing flow stresses associated with the final stages of deformation along the shear zone. Deformation experiments designed to simulate stress pulses associated with earthquakes resulted in a partial foam texture in samples that transitioned from deformation at high stress to low stress (Kidder et al., 2016). This process, wherein surface-energy-driven grain boundary migration and subsequent grain growth becomes more prominent with decreasing stress, would be expected to produce grain aggregates with a lower D-value while maintaining a similar average grain size (i.e. decreasing the bulk perimeter of the aggregate). The decrease in D-values near the core may reflect this process of decaying coseismic stresses associated with the passage of a rupture. In the shear-zone core (sample 41), we observe local patches of partial foam structure (Fig. 5d), but we have not observed this in other samples. The experiments of Kidder et al. (2016) also showed that the recrystallized grain size largely kept pace with the changing stresses. If the decrease in D-value is associated with decreasing stresses following passage of a rupture front, we might expect to see some increase in grain size within these samples. In the shear-zone core (sample 41) where we observe patches of partial foam structure, the average grain size is slightly larger (~12 μm) than in samples immediately outside the core in the QF rocks (~10 μm), though both are the same within uncertainty. Thus, it is possible that the core rocks underwent local, partial polygonization and grain growth due to changing stress in the seismic cycle as observed by Kidder et al. (2016).

Regardless of the mechanism driving the adjustment of grain boundaries, fluids introduced during coseismic damage may have been effective at increasing grain boundary mobility, thus allowing the perimeter length to adjust rapidly to changing deformation conditions. The concentration of fluid inclusions introduced to the interior of quartz grains during coseismic fragmentation and fluid infiltration has been shown to decrease within the mylonite zone, owing to subsequent recrystallization during the post- and interseismic periods (W.J. Song et al., 2020b). Recrystallization results in flushing the fluid inclusions from grain interiors to grain boundaries. This constant resupply of fluids along grain boundaries would enhance diffusion and keep boundaries mobile at lower temperatures in the middle crust. Whether or not similar D-values would have reflected transient events under dry conditions is unclear, as the effect of water on the D-value within quartz aggregates has not been experimentally tested.

5.3. Strain-rate estimates from D-values and flow laws combined with grain size piezometry

Geologic strain-rate estimates from geodesy and orogen-scale deformation predict strain rates on the order of $10^{-14\pm1}$ s^{-1} (e.g., Pfiffner and Ramsay, 1982; Kreemer et al., 2014), while strain-rate estimates from field outcrops of narrow ductile shear zones exhibit faster strain rates on the order of 10^{-13}–10^{-8} s^{-1} (e.g., Gueydan et al., 2005; Boutonnet et al., 2013; Viegas et al., 2016; Fagereng and Biggs, 2019). Strain-rate estimates along the SCSZ from the experimentally calibrated flow law of Lu and Jiang (2019) using the temperature-independent grain size piezometer of Stipp and Tullis (2003) plot at the strain rates of $10^{-14\pm1}$ s^{-1} (Fig. 8a). Application of this grain size piezometer with the naturally constrained low-stress flow law of Tokle et al. (2019) and the low-pressure flow law of Lusk et al. (2021) predicts faster strain rates on the order of 10^{-13}–10^{-11} s^{-1}, respectively, consistent with the range of strain rates predicted within localized shear zones. However, strain-rate estimates from D-values are ~1.5 orders of magnitude faster than those predicted by the flow law of Lusk et al. (2021). While the magnitude of the strain-rate estimates from D-values in our field area are within the previously cited range of strain-rate estimates from localized ductile shear zones, similar elevated strain-rate estimates are observed ubiquitously across studies implementing the GBD method.

The application of the temperature-dependent grain size piezometer of Shimizu (2012) to the flow laws of Lu and Jiang (2019), Tokle et al. (2019), and Lusk et al. (2021) results in a ~1.5 order of magnitude increase in calculated strain rates (Fig. 8b). This piezometer reduces the range in strain rate estimates between D-values and flow laws and nearly aligns with strain rates calculated from the flow law of Lusk et al. (2021). These results suggest that the discrepancy in strain rate estimates between the two methods may be resolved by fully accounting for temperature not only in the Arrhenius term of the flow law, but through the piezometer used to infer the flow stress. While there is currently no experimental evidence for quartz to resolve a temperature dependence on the relationship between average grain size and flow stress, these field results suggest a dependence that may be expressed at the lower temperature conditions in the continental crust, warranting future field investigations.

Another possible explanation of the consistently elevated strain rates derived from D-values may lie in the inherited texture and initial grain size of the starting materials used to derive Eq. (1). In contrast to the fine-grained to cryptocrystalline feather agate used in Takahashi et al. (1998), common starting materials are often coarser grained and isotropic (e.g., the Black Hills quartzite, characterized by an initial grain size on the order of ~70 μm) As deformation proceeds, grains in the agate must compete to increase toward a steady-state grain size, while those in coarser-grained starting materials undergo grain size reduction via bulge recrystallization and SGR recrystallization mechanisms. In metals, the initial grain size has been shown to impact microstructural evolution and the amount of strain to reach steady state (e.g., Huang and Logé, 2016). Materials exhibiting an initial grain size smaller than steady state require larger strains to reach steady state compared to materials with a larger initial grain size. Such differences in expected microstructural evolution may impact the empirically derived constants

and corresponding strain rate calculations between D-values and flow laws. Indeed, Takahashi et al. (1998) state that "from the stress-strain curves of Masuda and Fujimura (1981), the differential stress does not reach a steady state. As a result, we cannot discuss the power law relation between steady-state stress and average grain size due to inaccuracy and lack of measurement of axial forces". The lack of attainment of steady state, reported stresses, and grain sizes from the experiments of Takahashi et al. (1998) and Masuda and Fujimura (1981), combined with the initial grain size of their samples preclude us from confirming the hypothesized link between D-value, flow stress, and average grain size, suggesting the need for additional experimental calibrations of the GBD method.

5.4. Do D-values relate to measurements of surface irregularity?

The D-value has been referred to in the literature as a measure of the degree of roughness or serration of populations of grain boundaries (e.g., Hornbogen, 1989; Takahashi et al., 1998; Takahashi and Nagahama, 2001). If the average roundness of grains represents a measure of surface irregularity, we should expect a *negative* relationship between D-value and average roundness (i.e., high D-values and low average roundness correspond with more irregular grains), but our data show a positive relationship (Fig. 9d). Additionally, if $\overline{P}_{\mathrm{norm}}$ is a measure of surface irregularity, we should expect a positive relationship between D-values and $\overline{P}_{\mathrm{norm}}$, but our data show a negative relationship (Fig. 9e). Both average roundness and $\overline{P}_{\mathrm{norm}}$ are reasonable measures of surface irregularity as shown by the very strong negative correlation in Fig. 9f. These observations are the oppositive of what we would expect if D-value correlates with surface irregularity. The codependence of D-value with average grain size, average aspect ratio, and average roundness suggests a more complicated relationship with surface roughness than previously discussed.

6. Conclusions

(1) The spatial pattern of strain rates calculated from D-values are comparable to three published flow laws. While D-value strain rates are typically ~1–4 orders of magnitude faster than rates derived from these flow laws, consideration of the temperature-dependent piezometer of Shimizu (2012) reduces this discrepancy and results in near coincidence of rates from D-values and the low-pressure flow law of Lusk et al. (2021). Because the elevated strain rates from the GBD method may also stem from variations in the starting material used in the deformation experiments (e.g., agate vs. quartzite), future field work and experimental investigations across a range of deformation temperatures and quartz aggregate protoliths are necessary to address these observations.

(2) The relationship between D-value and average grain size in our field area suggests a strong micromechanical link to flow stress through the Zener-Hollomon parameter. Therefore, the D-value may also potentially be calibrated as a flow stress piezometer. Because the experiments of Takahashi et al. (1998) did not correct for friction in the deformation apparatus, experimental flow stresses were not available to confirm this relationship warranting future experimental investigation.

(3) The relationship between D-value and recrystallized grain size breaks down across the inner shear zone, coinciding with the concentration of coseismic damage and subsequent post-/interseismic creep. The decrease in D-values at near-uniform recrystallized grain size suggests that D-values may be more sensitive to transient deformation events than grain size. The decrease in D-value may reflect a shift in dominant deformation mechanism from dislocation creep to combined dislocation creep + grain-size sensitive creep.

(4) The relationship between D-value and shape properties in our field area demonstrates that the D-value is not an explicit measure of serration (roughness) of grain boundaries, but rather reflects an interdependence on grain size, aspect ratio and roundness.

CRediT authorship contribution statement

Erik K. Anderson: Writing – review & editing, Writing – original draft, Visualization, Validation, Methodology, Investigation, Formal analysis, Data curation, Conceptualization. **Won Joon Song:** Writing – review & editing, Validation, Methodology, Investigation, Data curation. **Scott E. Johnson:** Writing – review & editing, Supervision, Resources, Project administration, Funding acquisition. **Christopher C. Gerbi:** Writing – review & editing, Supervision.

Declaration of competing interest

The authors declare that they have no known competing financial interests or personal relationships that could have appeared to influence the work reported in this paper.

Acknowledgements

The authors gratefully acknowledge support from the National Science Foundation grants EAR-0820946, EAR-1727090, EAR-2150831 and EAR-2243658. We thank Steven Kidder and John Platt for guiding early thoughts on a previous iteration of this manuscript. Formal reviews by Alexander Lusk and Ichiko Shimizu led to important improvements to the current paper.

Appendix A. Supplementary data

Supplementary data to this article can be found online at https://doi.org/10.1016/j.jsg.2024.105330.

Appendices

A.1. Circularity

Circularity measures how close a shape is to a perfect circle (e.g., Wadell, 1932; Blott and Pye, 2008). While many definitions of circularity exist in the literature (Cox, 1927; Pentland, 1927; Wadell, 1933, 1935; Tickell, 1939; Riley, 1941; Janoo, 1998), we use the definition of Cox (1927):

$$C = \frac{4\pi A}{P^2} \tag{A1}$$

where C is circularity and P perimeter. The circularity of a particle varies between 0 and 1, with values of 1 representing a perfect circle. In Eq. (A1),

the dependence of circularity on the measured perimeter and area of a particle suggests two end-member conditions for reducing circularity: an increase in perimeter at constant area or a decrease in area at constant perimeter (Fig. 2d). Although circularity could be used in estimating surface irregularity, it is not enough to describe surface roughness because it can be reduced by increasing aspect ratio at constant perimeter.

A.2. Roundness (circularity corrected by aspect ratio)

Takashimizu and Iiyoshi (2016) defined a new parameter, "roundness", to quantify the surface irregularity of grain shapes. Note that their definition of roundness is different from that given by the International Organization for Standardization. While roundness commonly refers to the angularity of corners, they use the term to describe the presence/absence of surface irregularities. In the present study, we maintain their use of the term roundness. The upper panel of Fig. 2d shows how the roundness of a grain decreases from that of a perfect circle by increasing the perimeter at constant area. This configuration demonstrates a clear increase in the irregularity of the surface. In the lower panel of Fig. 2d, when the area decreases at constant perimeter, the aspect ratio increases, but the roundness from circle to ellipses does not change, despite decreasing circularity. This led Takashimizu and Iiyoshi (2016) to develop a new parameter of roundness that corrects the measured circularity of a grain using its aspect ratio. The correction was quantified using ImageJ and modelled ellipses with aspect ratio from 1 to 10 (Takashimizu and Iiyoshi, 2016), yielding:

$$r = C_I + (0.913 - C_{AR}) \tag{A2}$$

where r is roundness, C_I is the circularity measured in ImageJ using Eq. (A1), and C_{AR} is the circularity when the aspect ratio varies from that of a perfect circle. A sixth-order polynomial fit through the tested ellipses yielded the following regression for C_{AR}.

$$C_{AR} = 0.826261 + 0.337479 \bullet AR_I - 0.335455 \bullet AR_I^2 + 0.103642 \bullet AR_I^3 - 0.0155562 \bullet AR_I^4 + 0.00114582 \bullet AR_I^5 - 0.0000330834 \bullet AR_I^6 \tag{A3}$$

where AR_I is the aspect ratio of the best-fit ellipses calculated using ImageJ. The roundness of a particle varies between 0 and 1, with values of 1 representing a perfect circle. We use this definition of roundness to describe the surface roughness of quartz grains.

A.3. Average normalized ellipse perimeter ($\overline{P}_{norm}$)

Takeshita and El-Fakharani (2013) proposed another measure of grain boundary roughness that measures the deviation of the average perimeter of analyzed grains ($\overline{P}$) from the average perimeter of their best-fit ellipses ($\overline{P}_{\text{ellipse}}$). This measure, referred to as the average normalized ellipse perimeter ($\overline{P}_{\text{norm}}$), is defined as:

$$\overline{P}_{\text{norm}} = \frac{\overline{P}}{\overline{P}_{\text{ellipse}}} \tag{A4}$$

Perfectly elliptical grains have an average normalized ellipse perimeter of unity, increasing with increasing grain boundary roughness. For sake of thoroughness, we include this parameter in our discussion of grain shape and grain boundary roughness.

Data availability

Data will be made available on request.

References

Anderson, E.K., 2017. Constraining the Spatial Extent of Strain Localization at the Base of the Seismogenic Zone: A Case Study from the Sandhill Corner Shear Zone, vol. 2734. Electronic Theses and Dissertations, Maine, USA. https://digitalcommons.library.umaine.edu/etd/2734.

Anderson, E.K., Song, W.J., Johnson, S.E., Cruz-Uribe, A.M., 2021. Mica kink-band geometry as an indicator of coseismic dynamic loading. Earth Planet Sci. Lett. 567, 117000. https://doi.org/10.1016/j.epsl.2021.117000.

Baxter, E.F., DePaolo, D.J., 2004. Can metamorphic reactions proceed faster than bulk strain? Contrib. Mineral. Petrol. 146, 657–670. https://doi.org/10.1007/s00410-003-0525-3.

Bigerelle, M., Favergeon, J., Iost, A., 2012. Fractal dimension of grain boundary during heating. Comparison between images analyses and Monte Carlo simulation. Deflect Diffus. Forum 323–325, 133–138. https://dx.doi.org/10.4028/www.scientific.net/DDF.323-325.133.

Blott, S.J., Pye, K., 2008. Particle shape: a review and new methods of characterization and classification. Sedimentology 55, 31–63. https://doi.org/10.1111/j.1365-3091.2007.00892.x.

Boutonnet, E., Leloup, P.H., Sassier, C., Gardien, V., Ricard, Y., 2013. Ductile strain rate measurements document long-term strain localization in the continental crust. Geology 41 (1), 819–822. https://doi.org/10.1130/G33723.

Bürgmann, R., Dresen, G., 2008. Rheology of the lower crust and upper mantle: evidence from rock mechanics, geodesy, and field observations. Annu. Rev. Earth Planet Sci. 36, 531–567. https://doi.org/10.1146/annurev.earth.36.031207.124326.

Cawood, T.K., Platt, J.P., 2021. What controls the width of ductile shear zones? Tectonophysics 816, 229033. https://doi.org/10.1016/j.tecto.2021.229033.

Christensen, J.N., Rosenfeld, J.L., DePaolo, D.J., 1989. Rates of tectonometamorphic processes from rubidium and strontium isotopes in garnet. Science 244, 1465–1469. https://doi.org/10.1126/science.244.4911.1465.

Cox, E.P., 1927. A method of assigning numerical and percentage values to the degree of roundness of sand grains. J. Paleontol. 1, 179–183. https://www.jstor.org/stable/1298056.

Cross, A.J., Prior, D.J., Stipp, M., Kidder, S., 2017. The recrystallized grain size piezometer for quartz: an EBSD-based calibration. Geophys. Res. Lett. 44, 6667–6674. https://doi.org/10.1002/2017GL073836.

Fagereng, Å., Biggs, J., 2019. New perspectives on 'geological strain rates' calculated from both naturally deformed and actively deforming rocks. J. Struct. Geol. 125, 100–110. https://doi.org/10.1016/j.jsg.2018.10.004.

Faleiros, F.M., Moraes, R., Pavan, M., Campanha, G.A.C., 2016. A new empirical calibration of the quartz c-axis fabric opening-angle deformation thermometer. Tectonophysics 671, 173–182. https://doi.org/10.1016/j.tecto.2016.01.014.

Fukuda, J., Holyoke III, C.W., Kronenberg, A.K., 2018. Deformation of fine-grained quartz aggregates by mixed diffusion and dislocation creep. J. Geophys. Res. Solid Earth 123, 4676–4696. https://doi.org/10.1029/2017JB015133.

Fukuda, J., Shimizu, I., 2017. Theoretical derivation of flow laws for quartz dislocation creep: comparisons with experimental creep data and extrapolation to natural conditions using water fugacity corrections. J. Geophys. Res. Solid Earth 122, 5956–5971. https://doi.org/10.1002/2016JB013798.

Gerbi, C., West Jr., D.P., 2007. Use of U-Pb geochronology to identify successive, spatially overlapping tectonic episodes during Silurian-Devonian orogenesis in south-central Maine, USA. Geol. Soc. Am. Bull. 119 (1), 1218–1231. https://doi.org/10.1130/B26162.

Ghosh, S., Bose, S., Mandal, N., Dasgupta, S., 2016. Dynamic recrystallization mechanisms and their transition in the Daling Thrust (DT) zone, Darjeeling-Sikkim Himalaya. Tectonophysics 674, 166–181. https://doi.org/10.1016/j.tecto.2016.02.023.

Gleason, G.C., Tullis, J., 1995. A flow law for dislocation creep of quartz aggregates determined with the molten salt cell. Tectonophysics 247, 1–23. https://doi.org/10.1016/0040-1951(95)00011-B.

Goldsby, D.L., Kohlstedt, D.L., 2001. Superplastic deformation of ice: experimental observations. J. Geophys. Res. Solid Earth 106, 11017–11030. https://doi.org/10.1029/2000JB900336.

Grover, T.W., Fernandes, L.C., 2003. Bedrock geology of the weeks mills quadrangle, Maine. Maine geological survey, open-file map 03-49, color map, scale 1:24,000. https://digitalmaine.com/mgs_maps/31.

Gueydan, F., Mehl, C., Parra, T., 2005. Stress-strain rate history of a midcrustal shear zone and the onset of brittle deformation inferred from quartz recrystallized grain size. Geol. Soc. Spec. Publ. 243, 127–142. https://doi.org/10.1144/GSL.SP.2005.243.01.10.

Guidotti, C.V., 1989. Metamorphism in Maine: an overview. In: Tucker, R.D., Marvinney, R.G. (Eds.), Studies in Maine Geology: Volume 3 – Igneous and Metamorphic Geology. Maine Geological Survey, pp. 1–17. https://digitalmaine.com/mgs_publications/74.

Hatheway, R.B., 1971. Evidence for major faulting in south-central Maine. Geol. Soc. Am. Bull. 82, 253–258. https://doi.org/10.1130/0016-7606(1971)82[253:EFMFIS]2.0.CO;2.

Hirth, G., Teyssier, C., Dunlap, J.W., 2001. An evaluation of quartzite flow laws based on comparisons between experimentally and naturally deformed rocks. Int. J. Earth Sci. 90, 77–87. https://doi.org/10.1007/s005310000152.

Holyoke III, C.W., Kronenberg, A.K., 2010. Accurate differential stress measurement using the molten salt cell and solid salt assemblies in the Griggs apparatus with applications to strength, piezometers and rheology. Tectonophysics 494, 17–31. https://doi.org/10.1016/j.tecto.2010.08.001.

Hornbogen, E., 1987. Fractal analysis of grain boundaries in hot-worked poly-crystals. Z. Metallkde. 78, 622–625. https://doi.org/10.1515/ijmr-1987-780902.

Hornbogen, E., 1989. Fractals in microstructure of metals. Int. Mater. Rev. 34, 277–296. https://doi.org/10.1179/imr.1989.34.1.277.

Hu, J., Yu, X., Li, W., He, Y., Liu, N., Zhang, Y., 2021. Structural and rheological features of the northeastern Sanyang shear zone in the eastern Jiangnan orogen: indications for early Paleozoic orogeny in the South China Block. J. Struct. Geol. 153, 104472. https://doi.org/10.1016/j.jsg.2021.104472.

Huang, K., Logé, R.E., 2016. A review of dynamic recrystallization phenomena in metallic materials. Mater. Des. 111, 548–574. https://doi.org/10.1016/j.matdes.2016.09.012.

Hubbard, M.S., West Jr., D.P., Ludman, A., Guidotti, C.V., Lux, D.R., 1995. The Norumbega Fault Zone, Maine: a mid- to shallow-level crustal section within a transcurrent shear zone. Atl. Geol. 31, 109–116. https://doi.org/10.4138/2103.

Hussey, A.M.I.I., 1988. Lithotectonic stratigraphy, deformation, plutonism, and metamorphism, greater Casco Bay region, southwestern Maine. In: Tucker, R.D., Marvinney, R.G. (Eds.), Studies in Maine Geology: Volume 1 – Structure and Stratigraphy. Maine Geological Survey, pp. 17–34. https://digitalmaine.com/mgs_publications/47.

Janoo, V.C., 1998. Quantification of Shape, Angularity, and Surface Texture of Base Course Materials. U.S. Army Cold Regions Research and Engineering Laboratory. Special Report 98-1. https://rosap.ntl.bts.gov/view/dot/14065/dot_14065_DS1.pdf.

Johnson, S.E., Lenferink, H.J., Price, N.A., Marsh, J.H., Koons, P.O., West Jr., D.P., Beane, R., 2009. Clast-based kinematic vorticity gauges: the effects of slip at matrix/clast interfaces. J. Struct. Geol. 31, 1322–1339. https://doi.org/10.1016/j.jsg.2009.07.008.

Kalita, P., Goswami, T.K., Phukon, P., Srivastava, H.B., 2022. Deformation temperature, differential stress, and strain rate variation across the Bomdila Gneiss, western Arunachal Himalaya, India. Int. J. Earth Sci. 111, 607–622. https://doi.org/10.1007/s00531-021-02132-7.

Kidder, S., Avouac, J.-P., Chan, Y.-C., 2012. Constraints from rocks in the Taiwan orogen on crustal stress levels and rheology. J. Geophys. Res. Solid Earth 117, B09408. https://doi.org/10.1029/2012JB009303.

Kidder, S., Hirth, G., Avouac, J.-P., Behr, W., 2016. The influence of stress history on the grain size and microstructure of experimentally deformed quartzite. J. Struct. Geol. 83, 194–206. https://doi.org/10.1016/j.jsg.2015.12.004.

Kreemer, C., Blewitt, G., Klein, E.C., 2014. A geodetic plate motion and global strain rate model. Geochem. Geophys. Geosyst. 15, 3849–3889. https://doi.org/10.1002/2014GC005407.

Law, R.D., 2014. Deformation thermometry based on quartz *c*-axis fabrics and recrystallization microstructures: a review. J. Struct. Geol. 66, 129–161. https://doi.org/10.1016/j.jsg.2014.05.023.

Liang, C., Liu, Y., Neubauer, F., Bernroider, M., Jin, W., Li, W., Zeng, Z., Wen, Q., Zhao, Y., 2015. Structures, kinematic analysis, rheological parameters and temperature-pressure estimate of the Mesozoic Xingcheng-Taili ductile shear zone in the North China Craton. J. Struct. Geol. 78, 27–51. https://doi.org/10.1016/j.jsg.2015.06.007.

Liang, C., Liu, Y., Neubauer, F., Jin, W., Li, W., Heberer, B., Wen, Q., Li, J., Zhang, Li, 2017. Structural and rheological features of the western Liaoning metamorphic core complex corridor: indications for Late Mesozoic extension of the eastern North China Craton. J. Asian Earth Sci. 139, 142–164. https://doi.org/10.1016/j.jseaes.2017.01.013.

Lu, L.X., Jiang, D., 2019. Quartz flow law revisited: the significance of pressure dependence of the activation enthalpy. J. Geophys. Res. Solid Earth 124, 241–256. https://doi.org/10.1029/2018JB016226.

Luan, F.C., Paterson, M.S., 1992. Preparation and deformation of synthetic aggregates of quartz. J. Geophys. Res. Solid Earth 97, 301–320. https://doi.org/10.1029/91JB01748.

Ludman, A., Gibbons, S., 1999. Multistage shearing of the Deblois granite in the Kellyland fault zone, eastern Maine. In: Norumbega Fault System of the Northern Appalachians, vol. 331. Geological Society of America Special Paper, pp. 41–57. https://doi.org/10.1130/0-8137-2331-0.41.

Ludman, A., West Jr., D.P., 1999. Norumbega Fault System of the Northern Appalachians, vol. 331. Geological Society of America Special Paper. https://doi.org/10.1130/SPE331.

Lusk, A.D.J., Platt, J.P., 2020. The deep structure and rheology of a plate boundary-scale shear zone: constraints from an exhumed Caledonian shear zone, NW Scotland. Lithosphere 2020, 8824736. https://doi.org/10.2113/2020/8824736.

Lusk, A.D.J., Platt, J.P., Platt, J.A., 2021. Natural and experimental constraints on a flow law for dislocation-dominated creep in wet quartz. J. Geophys. Res. Solid Earth 126, e2020JB021302. https://doi.org/10.1029/2020JB021302.

Mamtani, M.A., 2010. Strain-rate estimation using fractal analysis of quartz grains in naturally deformed rocks. J. Geol. Soc. India 75, 202–209. https://doi.org/10.1007/s12594-010-0008-x.

Mandelbrot, B.B., 1977. Fractals: Form, Chance, and Dimension. W.H. Freeman and Company, San Fransisco.

Masuda, T., Fujimura, A., 1981. Microstructural development of fine-grained quartz aggregates by syntectonic recrystallization. Tectonophysics 72, 105–128. https://doi.org/10.1016/0040-1951(81)90089-5.

Müller, W., Aerden, D., Halliday, A.N., 2000. Isotopic dating of strain fringe increments: duration and rates of deformation in shear zones. Science 288, 2195–2198. https://doi.org/10.1126/science.288.5474.2195.

Nagahama, H., 1994. High–temperature viscoelastic behaviour and long time tail of rocks. In: Kruhl, J.H. (Ed.), Fractals and Dynamic Systems in Geoscience. Springer, Berlin, Heidelberg, pp. 121–129. https://doi.org/10.1007/978-3-662-07304-9_10.

Pentland, A., 1927. A method of measuring the angularity of sands. Proc. Trans. R. Soc. Can. 21, 43.

Pfiffner, O.A., Ramsay, J.G., 1982. Constraints on geological strain rates: arguments from finite strain states of naturally deformed rocks. J. Geophys. Res. Solid Earth 87, 311–321. https://doi.org/10.1029/JB087iB01p00311.

Pitzer, K.S., Sterner, S.M., 1994. Equations of state valid continuously from zero to extreme pressures for H_2O and CO_2. J. Chem. Phys. 101, 3111–3116. https://doi.org/10.1063/1.467624.

Platt, J.P., Behr, W.M., 2011. Grainsize evolution in ductile shear zones: implications for strain localization and the strength of the lithosphere. J. Struct. Geol. 33, 537–550. https://doi.org/10.1016/j.jsg.2011.01.018.

Price, N.A., Johnson, S.E., Gerbi, C.C., West Jr., D.P., 2012. Identifying deformed pseudotachylyte and its influence on the strength and evolution of a crustal shear zone at the base of the seismogenic zone. Tectonophysics 518–521, 63–83. https://doi.org/10.1016/j.tecto.2011.11.011.

Price, N.A., Song, W.J., Johnson, S.E., Gerbi, C.C., Beane, R.J., West Jr., D.P., 2016. Recrystallization fabrics of sheared quartz veins with a strong pre-existing crystallographic preferred orientation from a seismogenic shear zone. Tectonophysics 682, 214–236. https://doi.org/10.1016/j.tecto.2016.05.030.

Richter, B., Stünitz, H., Heilbronner, R., 2018. The brittle-to-viscous transition in polycrystalline quartz: an experimental study. J. Struct. Geol. 114, 1–21. https://doi.org/10.1016/j.jsg.2018.06.005.

Riley, N.A., 1941. Projection sphericity. J. Sediment. Res. 11, 94–95. https://doi.org/10.1306/D426910C-2B26-11D7-8648000102C1865D.

Rolandone, F., Bürgmann, R., Nadeau, R.M., 2004. The evolution of the seismic-aseismic transition during the earthquake cycle: constraints from the time-dependent depth distribution of aftershocks. Geophys. Res. Lett. 31, L23610. https://doi.org/10.1029/2004GL021379.

Rutter, E.H., Brodie, K.H., 2004. Experimental intracrystalline plastic flow in hot-pressed synthetic quartzite prepared from Brazilian quartz crystals. J. Struct. Geol. 26, 259–270. https://doi.org/10.1016/S0191-8141(03)00096-8.

Sassier, C., Leloup, P.H., Rubatto, D., Galland, O., Yue, Y., Lin, D., 2009. Direct measurement of strain rates in ductile shear zones: a new method based on syntectonic dikes. J. Geophys. Res. Solid Earth 114, B01406. https://doi.org/10.1029/2008JB005597.

Sato, K., Sakai, H., Kawakami, T., 2020. Distribution of ductile deformation around the Main Central Thrust zone at the frontal part of nappe in southeastern Nepal Himalaya. Isl. Arc 29, e12333. https://doi.org/10.1111/iar.12333.

Shimizu, I., 2008. Theories and applicability of grain size piezometers: the role of dynamic recrystallization mechanisms. J. Struct. Geol. 30, 899–917. https://doi.org/10.1016/j.jsg.2008.03.004.

Shimizu, I., 2011. Erratum to "Theories and applicability of grain size piezometers: the role of dynamic recrystallization mechanisms". J. Struct. Geol. 33, 1136–1137. https://doi.org/10.1016/j.jsg.2011.03.011 [J Struct Geol 30 (2008) 899–917].

Shimizu, I., 2012. Steady-state grain size in dynamic recrystallization of minerals. In: Sztwiertnia, K. (Ed.), Recrystallization. InTech, Rijeka, pp. 371–386. https://doi.org/10.5772/33701.

Shinevar, W.J., Behn, M.D., Hirth, G., 2015. Compositional dependence of lower crustal viscosity. Geophys. Res. Lett. 42, 8333–8340. https://doi.org/10.1002/2015GL065459.

Short, H.A., Johnson, S.E., 2006. Estimation of vorticity from fibrous calcite veins, central Maine, USA. J. Struct. Geol. 28, 1167–1182. https://doi.org/10.1016/j.jsg.2006.03.024.

Short, H.A., Kuiper, Y.D., Johnson, S.E., Jiang, D., 2011. Corrigendum to: "Estimation of vorticity from fibrous calcite veins, central Maine, USA" [J Struct Geol 2006; 28(7): 1167–1182]. J. Struct. Geol. 33, 59. https://doi.org/10.1016/j.jsg.2010.11.004.

Song, B.R., Johnson, S.E., Song, W.J., Gerbi, C.C., Yates, M.G., 2020a. Coseismic damage runs deep in continental strike-slip faults. Earth Planet Sci. Lett. 539, 116226. https://doi.org/10.1016/j.epsl.2020.116226.

Song, W.J., Johnson, S.E., Gerbi, C.C., 2020b. Quartz fluid inclusion abundance and off-fault damage in a deeply exhumed, strike-slip, seismogenic fault. J. Struct. Geol. 139, 104118. https://doi.org/10.1016/j.jsg.2020.104118.

Stipp, M., Stünitz, H., Heilbronner, R., Schmid, S.M., 2002. The eastern Tonale fault zone: a 'natural laboratory' for crystal plastic deformation of quartz over a temperature range from 250 to 700 °C. J. Struct. Geol. 24, 1861–1884. https://doi.org/10.1016/S0191-8141(02)00035-4.

Stipp, M., Tullis, J., 2003. The recrystallized grain size piezometer for quartz. Geophys. Res. Lett. 30, 2088. https://doi.org/10.1029/2003GL018444.

Streitenberger, P., Förster, D., Kolbe, G., Veit, P., 1995. The fractal geometry of grain boundaries in deformed and recovered zinc. Scr. Metall. Mater. 33, 541–546. https://doi.org/10.1016/0956-716X(95)00265-W.

Swanson, M.T., 1992. Late acadian-alleghenian transpressional deformation: evidence from asymmetric boudinage in the casco bay area, coastal Maine. J. Struct. Geol. 14, 323–341. https://doi.org/10.1016/0191-8141(92)90090-J.

Swanson, M.T., 1999. Kinematic indicators for regional dextral shear along the Norumbega fault system in the Casco Bay area, coastal Maine. In: Norumbega Fault System of the Northern Appalachians, vol. 331. Geological Society of America Special Paper, pp. 1–23. https://doi.org/10.1130/0-8137-2331-0.1.

Swanson, M.T., 2006a. Late Paleozoic strike-slip faults and related vein arrays of Cape Elizabeth, Maine. J. Struct. Geol. 28, 456–473. https://doi.org/10.1016/j.jsg.2005.12.009.

Swanson, M.T., 2006b. Pseudotachylyte-bearing strike-slip faults in mylonitic host rocks, Fort Foster brittle zone, Kittery, Maine. In: Abercrombie, R., McGarr, A., Di Toro, G., Kanamori, H. (Eds.), Earthquakes: Radiated Energy and the Physics of Faulting, vol. 170. Geophysical Monograph Series, pp. 167–179. https://doi.org/10.1029/170GM17.

Takahashi, M., Nagahama, H., 2001. The sections' fractal dimension of grain boundary. Appl. Surf. Sci. 182, 297–301. https://doi.org/10.1016/S0169-4332(01)00417-2.

Takahashi, M., Nagahama, H., Masuda, T., Fujimura, A., 1998. Fractal analysis of experimentally, dynamically recrystallized quartz grains and its possible application as a strain rate meter. J. Struct. Geol. 20, 269–275. https://doi.org/10.1016/S0191-8141(97)00072-2.

Takashimizu, Y., Iiyoshi, M., 2016. New parameter of roundness *R*: circularity corrected by aspect ratio. Prog. Earth Planet. Sci. 3, 2. https://doi.org/10.1186/s40645-015-0078-x.

Takeshita, T., El-Fakharani, A.-H., 2013. Coupled micro-faulting and pressure solution creep overprinted on quartz schist deformed by intracrystalline plasticity during exhumation of the Sambagawa metamorphic rocks, southwest Japan. J. Struct. Geol. 46, 142–157. https://doi.org/10.1016/j.jsg.2012.09.014.

Tanaka, M., Iizuka, H., 1991. Characterization of grain boundaries by fractal geometry and creep-rupture properties of heat-resistant alloys. Z. Metallkde. 82, 442–447. https://doi.org/10.1515/ijmr-1991-820604.

Tanaka, M., Kayama, A., Ito, Y., Kato, R., 1998. Effects of the creep deformation on the fractal dimension of the grain boundaries in an austenite steel. J. Mater. Sci. 33, 3351–3359. https://doi.org/10.1023/A:1013241531412.

Tickell, F.G., 1939. The Examination of Fragmental Rocks, second ed. Stanford University Press, Stanford University, Calif.

Tokle, L., Hirth, G., Behr, W.M., 2019. Flow laws and fabric transitions in wet quartzite. Earth Planet Sci. Lett. 505, 152–161. https://doi.org/10.1016/j.epsl.2018.10.017.

Tucker, R.D., Osberg, P.H., Berry IV, H.N., 2001. The geology of a part of Acadia and the nature of the Acadian orogeny across Central and Eastern Maine. Am. J. Sci. 301, 205–260. https://doi.org/10.2475/ajs.301.3.205.

Viegas, G., Menegon, L., Archanjo, C., 2016. Brittle grain-size reduction of feldspar, phase mixing and strain localization in granitoids at mid-crustal conditions (Pernambuco shear zone, NE Brazil). Solid Earth 7, 375–396. https://doi.org/10.5194/se-7-375-2016.

Wadell, H., 1932. Volume, shape, and roundness of rock particles. J. Geol. 40, 443–451. https://www.jstor.org/stable/30058012.

Wadell, H., 1933. Sphericity and roundness of rock particles. J. Geol. 41, 310–331. https://www.jstor.org/stable/30058841.

Wadell, H., 1935. Volume, shape, and roundness of quartz particles. J. Geol. 43, 250–280. https://www.jstor.org/stable/30056250.

Wang, C., Ludman, A., 2004. Deformation conditions, kinematics, and displacement history of shallow crustal ductile shearing in the Norumbega fault system in the Northern Appalachians, eastern Maine. Tectonophysics 384, 129–148. https://doi.org/10.1016/j.tecto.2004.03.013.

Wang, X., Dong, L., Xiong, L., 1990. The change of fractal dimensionality in the recovery and recrystallisation process. J. Phys. Condens. Matter 2, 3879–3884. https://doi.org/10.1088/0953-8984/2/16/017.

Wang, Z., Liu, X., He, Y., Xie, J., 2010. A fractal-based model for the microstructure evolution of silicon bronze wires fabricated by dieless drawing. Int. J. Miner. Metall. Mater. 17, 770–776. https://doi.org/10.1007/s12613-010-0387-4.

Watanabe, T., Tsurekawa, S., 2004. Toughening of brittle materials by grain boundary engineering. Mater. Sci. Eng. A 387–389, 447–455. https://doi.org/10.1016/j.msea.2004.01.140.

West Jr., D.P., Beal, H.M., Grover, T.W., 2003. Silurian deformation and metamorphism of Ordovician arc rocks of the Casco Bay Group, south-central Maine. Can. J. Earth Sci. 40, 887–905. https://doi.org/10.1139/e03-021.

West Jr., D.P., Hubbard, M.S., 1997. Progressive localization of deformation during exhumation of a major strike-slip shear zone: Norumbega fault zone, south-central Maine, USA. Tectonophysics 273, 185–201. https://doi.org/10.1016/S0040-1951(96)00306-X.

West Jr., D.P., Lux, D.R., 1993. Dating mylonitic deformation by the ^{40}Ar-^{39}Ar method: an example from the Norumbega Fault Zone, Maine. Earth Planet Sci. Lett. 120, 221–237. https://doi.org/10.1016/0012-821X(93)90241-Z.

West Jr., D.P., Lux, D.R., Hussey, A.M.I.I., 1993. Contrasting thermal histories across the Flying Point fault, southwestern Maine: evidence for Mesozoic displacement. Geol. Soc. Am. Bull. 105 (2), 1478–1490. https://doi.org/10.1130/0016-7606(1993)105<1478:CTHATF>2.3.CO.

West Jr., D.P., Peterman, E.M., 2004. Bedrock geology of the razorville quadrangle, Maine. Maine geological survey, open-file map 04-29, color map, scale 1:24,000. http://digitalmaine.com/mgs_maps/40.

West Jr., D.P., Peterman, E.M., Chen, J., 2021. Silurian-Devonian tectonic evolution of mid-coastal Maine, U.S.A.: Details of polyphase orogenic processes. Am. J. Sci. 321, 458–489. https://doi.org/10.2475/04.2021.03.